Monthly Notices of the ROYAL ASTRONOMICAL SOCIETY

MNRAS **453,** 414–438 (2015) doi:10.1093/mnras/stv1619

Resolving structure of the disc around HD100546 at 7 mm with ATCA

C. M. Wright,[1⋆] S. T. Maddison,[2⋆] D. J. Wilner,[3] M. G. Burton,[4] D. Lommen,[5] E. F. van Dishoeck,[6] P. Pinilla,[6] T. L. Bourke,[7] F. Menard[8] and C. Walsh[6]

[1]*School of Physical, Environmental and Mathematical Sciences, UNSW@ADFA, Canberra ACT 2600, Australia*
[2]*Centre for Astrophysics & Supercomputing, Swinburne University, PO Box 218, Hawthorn, VIC 3122, Australia*
[3]*Harvard–Smithsonian Center for Astrophysics, 60 Garden Street, Cambridge, MA 02138, USA*
[4]*School of Physics, University of New South Wales, Sydney, NSW 2000, Australia*
[5]*Hwa Chong Institution, 661 Bukit Timah Road, 269734, Singapore*
[6]*Leiden Observatory, Leiden University, PO Box 9531, NL-2300 RA Leiden, the Netherlands*
[7]*SKA Organization, Jodrell Bank Observatory, Lower Withington, Macclesfield, Cheshire SK11 9DL, UK*
[8]*Millenium Nucleus 'Protoplanetary Disks in ALMA Early Science', Universidad de Chile, Casilla 36-D, Santiago, Chile*

Accepted 2015 July 15. Received 2015 July 15; in original form 2015 March 12

ABSTRACT

There is much evidence that planet formation is occurring in the disc around the Herbig Be star HD100546. To learn more about the processes occurring in this disc, we conducted high-resolution imaging at 43/45 GHz with the Australia Telescope Compact Array. Multiple array configurations were used, providing a best spatial resolution of ∼0.15 arcsec, or 15 au at HD100546's distance of ∼100 pc. Significant structure is revealed, but its precise form is dependent on the $u - v$ plane sampling used for the image reconstruction. At a resolution of ≤30 au, we detected an inner gap in the disc with a radius of ∼25 au and a position angle approximately along the known disc major axis. With different weighting, and an achieved resolution of ∼15 au, emission appears at the centre and the disc takes on the shape of an incomplete ring, much like a horseshoe, again with a gap radius of ∼25 au. The position angle of the disc major axis and its inclination from face-on are determined to be 140° ± 5° and 40° ± 5°, respectively. The ∼25 au gap radius is confirmed by a null in the real part of the binned visibilities at 320 ± 10 kλ, whilst the non-axisymmetric nature is also confirmed through significant structure in the imaginary component. The emission mechanism at the central peak is most likely to be free–free emission from a stellar or disc wind. Overall our data support the picture of at least one, but probably several, giant planets orbiting HD100546 within 25 au.

Key words: protoplanetary discs – circumstellar matter – planetary systems – stars: pre-main-sequence – radio continuum: stars.

1 INTRODUCTION

As well as being the reservoir of material accreting on to young stars, discs also provide the raw material for the building of a planetary system. A diverse range of physical and chemical processes must however occur before the dilute mixture of gas and dust is transformed into discrete rocky and gas planets. Yet despite the discovery of thousands of extrasolar planets over the last few decades, with an exotic suite of orbital and physical properties, plus detailed studies of our own Solar system, our understanding of the planet formation process remains incomplete.

In order to learn more about the early stages of planet formation, we have undertaken an extensive observing programme from the millimetre to centimetre range of several Herbig star+disc systems, including HD100546, using the Australia Telescope Compact Array (ATCA).[1] Observations at millimetre wavelengths are especially important as they probe the colder regions of the disc – the outer parts and mid-plane – where the bulk of the mass resides (e.g. Beckwith & Sargent 1991).

HD100546 is a Herbig Be star which displays a range of phenomena suggesting it may be the host of a planetary system in the early stage of its formation and evolution. Its age is not well determined, but is likely to be in the range of 3.5–10 Myr. The lower end comes from Manoj et al. (2006) and the upper from van den Ancker et al.

⋆ E-mail: c.wright@adfa.edu.au (CMW); smaddison@swin.edu.au (STM)

[1] The ATCA is part of the Australia Telescope which is funded by the Commonwealth of Australia for operation as a National Facility managed by CSIRO.

(1997). The old and new *Hipparcos* distances are 103^{+7}_{-6} pc (van den Ancker et al. 1997) and 97 ± 4 pc (van Leeuwen 2007), but we simply use 100 pc throughout this paper. It is situated on the edge of, and associated with, the dark cloud DC296.2–7.9 (Hu, The & de Winter 1989; Vieira, Pogodin & Franco 1999). HD100546 and its environs have been extensively studied over the last 20 yr as its potential similarity to the early solar nebula has been gradually revealed. Its close proximity allows many phenomena to be resolved at the few to few tens of au scale.

An optical and near-IR scattering disc has been detected from about 15 out to 500 au by many authors, including Pantin, Waelkens & Lagage (2000), Augereau et al. (2001) and Quanz et al. (2011). Spiral and dark lane structure was also observed within this scattering disc – from about 150 to 300 au – by Grady et al. (2001), Ardila et al. (2007), Boccaletti et al. (2013) and Avenhaus et al. (2014b). Thermal dust emission out to a few tens of au was detected by mid-infrared nulling interferometry and direct imaging observations of the disc by Liu et al. (2003), Leinert et al. (2004) and Mulders et al. (2011).

Besides the several hundred au radius disc, an extended envelope has also been detected out to about 1000 au via dust scattering in the optical regime by Grady et al. (2001) and Ardila et al. (2007). The latter find the colours of the envelope to be similar to those of Kuiper Belt Objects (KBOs) in our own Solar system. They suggest that the HD100546 disc may be transitional between a pre-main-sequence disc and one dominated by planetesimal collisions, making it an important target for our overall understanding of disc evolution.

HD100546 has a remarkable 2–45 μm spectrum measured by the Infrared Space Observatory (ISO; Malfait et al. 1998b). Its spectrum resembles that of comet Hale–Bopp, with a wealth of features indicative of a large fraction of crystalline silicates, predominantly forsterite. Mulders et al. (2011) estimate a crystalline mass fraction of 40–60 per cent, located predominantly between 13 and 20 au. This suggests that a process has occurred in the HD100546 disc to crystallise the dust, possibly common to that which occurred in our own Solar system during its formation.

Perhaps not surprisingly, independent observations have indicated the presence of at least one massive body. Grady et al. (2005) detect a central cavity extending about 13 au from the star, much larger than can be explained by dust sublimation and with a centroid offset from the star by 5 au along the disc major axis. They interpret this cavity as having been dynamically sculpted by one or more bodies, favouring a giant planet. Liu et al. (2003, 2007) also favour a giant (proto)planet based on their inference of a large inner gap at less than 10 au from mid-infrared imaging and nulling interferometry. A 13 au radius cavity has also been inferred from observations of CO and OH infrared ro-vibrational transitions by several authors (Brittain, Najita & Carr 2009; van der Plas et al. 2009; Liskowsky et al. 2012; Brittain et al. 2013, 2014) and is also consistent with radiative transfer modelling of the near- to far-IR spectral energy distribution (SED; Bouwman et al. 2003; Benisty et al. 2010; Mulders et al. 2011; Tatulli et al. 2011; Mulders et al. 2013a,b).

From spatially and velocity resolved [O I] 6300 Å data, Acke & van den Ancker (2006) infer the mass of the body clearing the cavity to be around 20 Jupiter masses (hereafter M_J), orbiting at about 6.5 au. This puts it in the brown dwarf rather than planet realm. Hydrodynamic simulations by Tatulli et al. (2011) instead find that a 1–8 M_J body placed at 8 au can produce the 13 au radius cavity within a time-scale shorter than the age of the system. Most recently, using a combination of coronagraphy and polarimetric imaging Quanz et al. (2013a) claim to have directly detected a giant protoplanet at a radius of about 70 au. Notably, this could not be the body responsible for the inner clearing, and thus a picture of a planetary system begins to emerge.

There has been comparatively little work on the millimetre properties of the HD100546 disc. It was found to be a strong source of 1.3 mm dust emission by Henning et al. (1994, 1998) using the Swedish-ESO Submillimetre Telescope (SEST) single dish telescope. They inferred the presence of a disc – embedded within a core-envelope structure – since their spherical geometry radiative transfer model failed to reproduce the 1.3 mm flux by an order of magnitude. Direct evidence for a compact disc was provided by ATCA 3.4 mm observations of Wilner et al. (2003). More recently Walsh et al. (2014) and Pineda et al. (2014) presented ALMA observations of the disc at 870 μm (plus 990 μm in Walsh et al.) using the same data set, which provided evidence for a central disc cavity.

The 7 mm data we present is part of a much larger observing campaign of HD100546 which we have conducted with ATCA over the last decade, ranging from a frequency of 4.8 to 95.5 GHz (wavelength of 62.5 to 3.1 mm). The main body of this paper considers the high-resolution 7 mm imaging, presenting the first millimetre picture of the hole within the HD100546 disc. Where appropriate, to support conclusions we will quote results from the larger data set, but which itself is confined to several appendices only available online.

2 OBSERVATIONS AND DATA REDUCTION

We used the ATCA to observe HD100546 at multiple frequencies within the 3, 7 and 16 mm bands, as well as at 4.8 and 8.64 GHz. Several array configurations were used from 2002 31 May through to 2012 27 June. Table 1 contains a log of the 7 mm observations, which provided the best imaging data. Tables A1, A2 and A3 of Appendix A – only available online as supplementary material – list the 3 mm, 16 mm and 3+6 cm observational details. Before 2009, the continuum mode of the ATCA correlator had a bandwidth of 128 MHz with 32 channels to give 4 MHz per channel in two sidebands. In early 2009, a new correlator was commissioned at ATCA, the Compact Array Broad-band Backend, or CABB (Wilson et al. 2011). For each sideband, this provided a bandwidth of 2 GHz with 2024 channels of 1 MHz each. For the 7 mm CABB data, the two sidebands were centred at 43 and 45 GHz.

Up until 2010 May, the complex gains were derived from observations of the quasar PKS B1057−797, separated by about 10° on the sky from HD100546's position. In 2010 and 2012, the quasar j1147−653 was used, which is much closer on the sky to HD100546 and so provided a better representation of the phase conditions along the latter's line of sight. The gain calibrator was typically observed every 5–15 mins for between 1 and 3 mins duration, dependent on atmospheric conditions. Pointing checks were also made on the quasar every 60–90 mins.

The bandpass response was determined from 15 min observations of one or more of the quasars PKS B0537−441, PKS B1253−055 and PKS B1921−293. As seen in Table 1 in most cases flux calibration was performed using Uranus, though Mars and ATCA's primary cm-band flux calibrator, the quasar 1934−638, were also used. 15 min observations were typically made. The secondary calibrators 1057−797 or j1147−653 were used on occasion after bootstrapping to one of the aforementioned primary calibrators within a few days or weeks. Given their intrinsic (and typically non-periodic) variability this approach obviously has some risk. See for instance

Table 1. 7 mm ATCA observations of HD100546.

Date UT	ν_1 (MHz)	F_1 (mJy)	ν_2 (MHz)	F_2 (mJy)	Phase cal. elev. (°)	Flux cal., elev. (°)	T_{int} (mins)	Config	Min, Max baselines (m)
2007 Oct 4	41 000	7.32 ± 0.17 P	43 000	7.93 ± 0.18 P	35–40	Uranus, 65	140	H75	31, 89 (4408)
		7.27 ± 0.30 G		7.97 ± 0.36 G					
2007 Oct 4	**41 000**	**7.84 ± 0.18 P**	**43 000**	**8.58 ± 0.20 P**	35–40	Uranus, 50	140	H75	31, 89 (4408)
		7.77 ± 0.36 G		**8.80 ± 0.40 G**					
2007 Oct 5	41 000	4.88 ± 0.31 P	43 000	4.96 ± 0.33 P	40	Uranus, 50	60	H75	31, 89 (4408)
		5.57 ± 0.73 G		6.40 ± 0.83 G					
2008 Jun 27	42 944	9.02 ± 0.41 G	44 992	9.61 ± 0.42 G	37–40	Mars, 28	260	1.5B	31, 4301
2009 May 30	43 000	6.10 ± 0.08 P	45 000	6.69 ± 0.10 P	38–40	Uranus, 42	60	H214D	82, 247 (4500)
		7.94 ± 0.20 G		8.25 ± 0.25 G					
2009 May 31	**43 000**	**7.99 ± 0.12 P**	**45 000**	**8.36 ± 0.16 P**	35–31	Uranus, 27	60	H214D	82, 247 (4500)
		8.80 ± 0.27 G		**8.79 ± 0.34 G**					
2009 Aug 1	43 000	5.47 ± 0.05 G	45 000	5.86 ± 0.07 G	40–30	1934-638, 48	280	1.5A	153, 4469
2009 Aug 3	43 000	6.81 ± 0.26 G	45 000	7.50 ± 0.46 G	25–22	Uranus, 55	80	1.5A	153, 4469
2009 Aug 15	43 000	5.89 ± 0.17 G	45 000	6.67 ± 0.23 G	30–22	Uranus, 42	190	6D	77, 5878
2009 Aug 26	43 000	6.56 ± 0.15 G	45 000	7.04 ± 0.19 G	28–34	1057−797[a]	120	6D	77, 5878
2010 May 3	43 000	3.65 ± 0.13 G	45 000	3.63 ± 0.16 G	24–52	1934−638, 55	383	6A	337, 5939
2012 May 23	43 000	8.42 ± 0.28 G	45 000	9.73 ± 0.40 G	13–52	j1147−653	545	6D	77, 5878[b]
2012 Jun 20	43 000	6.73 ± 0.07 G	45 000	7.36 ± 0.09 G	12–52	Uranus, 40	495	6D	77, 5878

[a]Flux used for 1057−797 was 1.945 Jy at both frequencies from observation on 2009 August 15.
[b]The 2012 May 23 observations did not have antenna's 2 and 3 available. P and G refer to Point and Gaussian source models in MIRIAD's UVFIT. Numbers in bold are our best estimates of the 41, 43 and 45 GHz total fluxes of HD100546. A flux of 8.5 ± 0.5 mJy is recommended at 44 GHz, dominated by thermal dust emission but with a minor contribution from free–free emission. See Appendix C for details (only available online as supplementary material).

Torniainen et al. (2005). All subsequent data reduction, including calibration and imaging, was performed with the MIRIAD software (Sault, Teuben & Wright 1995).

Appendix A (only available online) contains a more detailed description of flux calibration issues. But we point out here the first two entries in Table 1 are the same data set but with a different planet observation – taken about 10 h before and after the science track – for the flux calibration. This shows a change in total flux of between 0.5 and 0.8 mJy. We have chosen the second observation as being closer to the true flux since the planet was at a similar elevation to the science track.

In order to combine the CABB 7 mm data from all array configurations, we first determined offsets from the phase centre using the UVFIT routine in MIRIAD and an elliptical Gaussian model. Such offsets were the result of several factors, including purposefully setting the phase centre off the nominal stellar position by some fraction of a synthesized beamwidth (to avoid artefacts due to DC offset and/or sampler harmonics errors, as stipulated in the ATCA Users Guide[2]), proper motion of HD100546, and telescope pointing and/or tracking errors. The respective data sets were then corrected to a common phase centre using MIRIAD's UVEDIT. That the input offset was successful in each case was demonstrated by the residual offsets all being less than ∼0.04 arcsec, and mostly ∼0.01 arcsec, when again fit with an elliptical Gaussian in UVFIT. A similar methodology for combining separate tracks has recently been applied to other discs, such as that of TW Hya in Andrews et al. (2012) and LkHα 330 in Isella et al. (2013).

Treating each sideband separately, the respective configurations were combined with MIRIAD's UVCAT, fourier inverted, deconvolved with CLEAN and restored with a synthesized beam to produce a final image. The two independent frequency bands produced extremely consistent images so were combined to enhance the signal to noise (S/N), and the 'effective' frequency is referred to here as 44 GHz. As a further consistency check, the same process was also applied to all the individual data sets. The longest baseline was almost 6 km, and the achieved resolution ∼0.15–0.50 arcsec. This corresponds to ∼15–50 au at the distance of HD100546, and depended on the weighting applied during the inversion. This weighting was varied from natural through to uniform and superuniform, which apply progressively more weight to longer baselines to give higher resolution but at the cost of S/N. Our data provides some of the highest resolution millimetre images ever obtained of a circumstellar disc.

[2] www.narrabri.atnf.csiro.au/observing/users_guide/html/atug.html

3 RESULTS

3.1 Fluxes

Derived fluxes for HD100546 in both sidebands are presented in Table 1, obtained in the $u - v$ plane with MIRIAD's UVFIT and point or elliptical Gaussian source models. Note that in 2007 October, the frequency pair was 41/43 GHz, whilst subsequently it was 43/45 GHz. There are some differences in flux between tracks based solely on the statistical uncertainties, but it is unlikely to be due to intrinsic source variability. Whilst we have observed short term (i.e. hourly, factor of 2–3) flux variability for HD100546 at 4.8 and 8.64 GHz, we have not detected variability at 19 GHz or 90–95 GHz (see Appendices A and B only available online).

Thus, the different 7 mm fluxes seen in Table 1 probably reflect one or more of the absolute flux calibration accuracy, 'missing' extended flux in the long baseline configurations due to inadequate $u - v$ plane sampling, and/or a Gaussian not being a good representation of the source morphology. Specifically note that the fluxes measured on 2007 October 5 and 2010 May 3 are about half that typically measured. But these observations had the worst overall phase stability and in the case of 2010 May 3 the longest minimum baseline length.

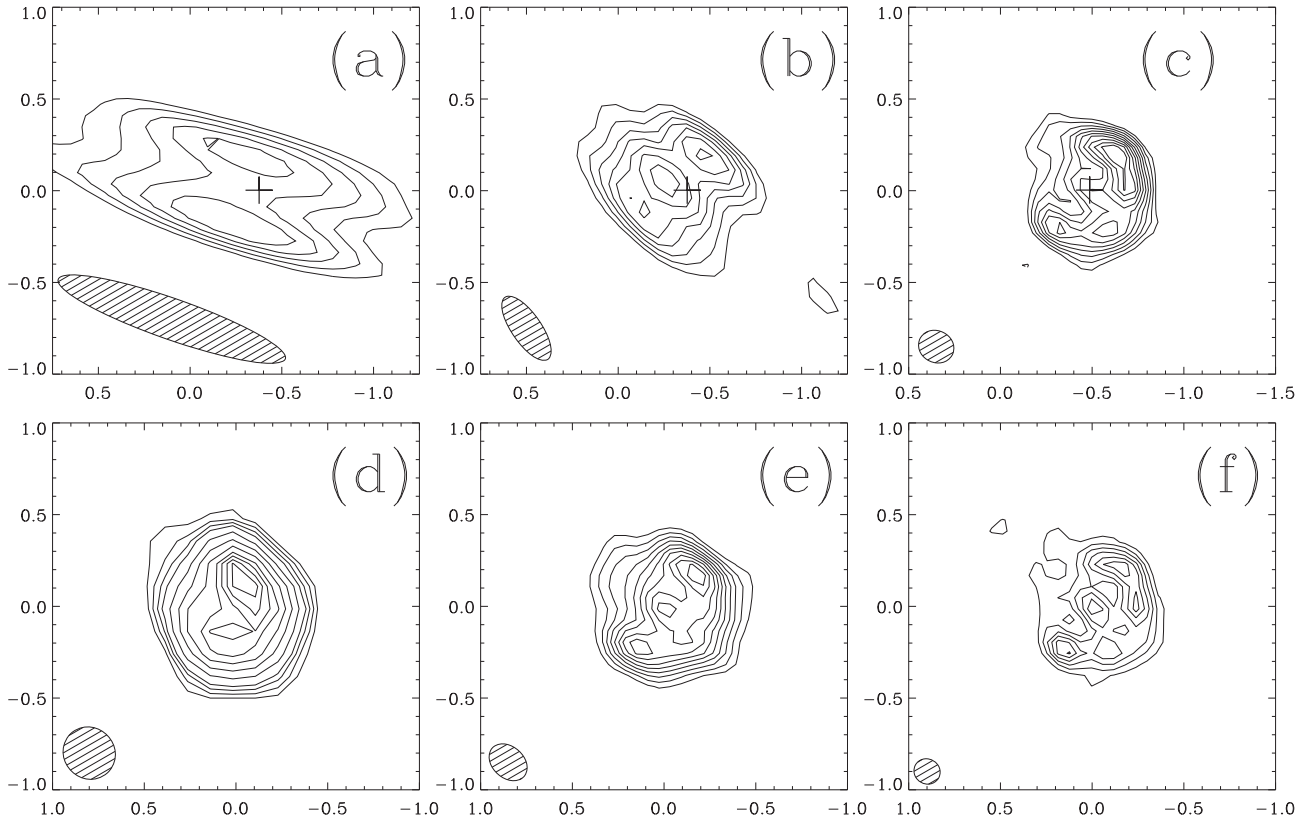

Figure 1. Images of HD100546, with offsets in arcseconds. North is up and east to the left. For the top row images the offsets are from the J2000 position. The cross on these images shows the expected position of HD100546 at the time of the observation, using its established proper motion over 9.7 yr for (a) and (b) and 12.5 yr for (c). For the bottom row images, the (0,0) position is made to coincide with the central emission peak. (a) Combined 43 and 45 GHz, naturally weighted in the 6D configuration on 2009 August 26, with a synthesized beam of 1.31 × 0.22 arcsec at PA = 70.°7. Contours are scaled by the rms of 0.054 mJy beam^{-1}, with levels at 7σ–15σ in steps of 2. (b) Combined 43 and 45 GHz, uniformly weighted in the 1.5A configuration on 2009 August 1, with a synthesized beam of 0.44 × 0.17 arcsec at PA = 34.°6. Contours are scaled by the rms of 0.039 mJy beam^{-1}, with levels at 7σ, 9σ, 11σ, 13σ, 15σ, 17.5σ, 20σ. (c) Combined 43 and 45 GHz, uniformly weighted in the 6D configuration on 2012 June 20, with a synthesized beam of 0.20 × 0.18 arcsec at PA = 74.°5. Contours are scaled by the rms of 0.030 mJy beam^{-1}, with levels at 6σ–24σ in steps of 2. (d) 43 GHz superuniformly weighted from all CABB configurations combined, but without antenna 6 baselines. The synthesized beam size is 0.29 × 0.28 arcsec at PA = 44.°0. Contours are scaled by the rms of 0.029 mJy beam^{-1}, with levels at 5σ, 7σ, 9σ, 11σ, 15σ, 20σ, 25σ, 30σ, 33σ, 36σ, 39σ. (e) 43 GHz uniformly weighted from all CABB configurations combined, with a synthesized beam of 0.23 × 0.17 arcsec at PA = 48.°2. Contours are scaled by the rms of 0.024 mJy beam^{-1}, with levels at 5σ–23σ in steps of 2. (f) 43 GHz superuniformly weighted from all CABB configurations combined, with a synthesized beam of 0.15 × 0.14 arcsec at PA = 59.°2. Contours are scaled by the rms of 0.032 mJy beam^{-1}, with levels at 3σ–13σ in steps of 2.

With these considerations in mind, the fluxes measured in the H75 and H214 compact hybrid configurations on 2007 October 4 and 2009 May 31, respectively, probably represent the best total flux estimates. These are in boldface in Table 1. The sky conditions were good and importantly stable over these relatively short observations, and HD100546 remained unresolved. The latter is demonstrated by the fact that there is little difference, within the respective uncertainties, between the fluxes measured using a point source or elliptical Gaussian. A 44 GHz flux of 8.5 ± 0.5 mJy is recommended.

Of the extended configurations, the 2012 June 20 track was conducted in the best conditions, which were also relatively stable over the course of the observation. Indeed, this track was conducted as part of the commissioning of ATCA's water vapour radiometers (WVR), but the WVR-based phase correction provided no substantive improvement over that of the quasar-based correction (Jones, Indermuehle & Burton 2012). This data set produced extremely good high-resolution images, which were clearly superior to those from other tracks.

3.2 Images

Figs 1(a), (b) and (c), respectively, show combined 43/45 GHz images acquired from single tracks on 2009 August 26 in the 6D configuration, 2009 August 1 in 1.5A, and 2012 June 20 in 6D. Figs 1(d), (e) and (f) instead show 43 GHz images derived from combining the data from all array configurations with CABB. In Figs 1(a), (b) and (c), the offsets are in arcseconds from the nominal J2000 position of RA = 11:33:25.44058 and δ = −70:11:41.2363. The centroid in these images is clearly shifted west of this position (with little or no N-S offset), which is accounted for by the known proper motion of HD100546 of ∼−39 mas yr^{-1} in RA and 0.29 mas yr^{-1} in declination (position marked by a cross; van Leeuwen 2007). Being combined images, Figs 1(d) and (e) and (f) have instead been shifted to a common position of the central emission peak.

Only for the 2012 June 20 data set in Fig. 1(c), with the best phase correction and $u - v$ coverage, does the cross coincide with the emission centroid. For the 2009 August 1 and 26 data sets in Figs 1(b) and (a), respectively, the offset of HD100546 is smaller than would be predicted from its proper motion over 9.7 yr. But in

both cases the beam is highly elongated, and the offset between the centroid and the cross is along the direction of the elongation. We thus conclude in these cases that the centroid is consistent with the expected proper motion.

Both single-track and combined images are shown because they demonstrate the important point that the same structure is observed, thus providing high confidence in the fidelity of the combination, especially the crucial aspects of relative astrometry and flux calibration. These considerations become relevant for the self-calibration process presented in the next section.

Perhaps the most obvious features of the HD100546 disc demonstrated by Fig. 1 is that it is very compact but with significant internal structure. Fig. 1 shows unequivocally that, depending on the beam size and shape (i.e. the resolution along particular directions), the structure observed in the HD100546 disc at 7 mm is noticeably different. For instance, immediately apparent from all the images is a hole in the disc, but the presence or otherwise of a central peak is dependent on resolution (or equivalently the $u - v$ plane coverage).

At a resolution of ∼0.20–0.30 arcsec along the known disc major axis, as in Fig. 1(a) and (d), or 20–30 au at the distance of HD100546, two peaks are observed, separated by ∼0.50 arcsec. The mid-point of the axis joining the two peaks is coincident with the stellar position, and the NW emission peak is brighter than the SE peak. But at ∼0.15 arcsec resolution along the disc major axis, or 15 au, as in Figs 1(b), (c), (e) and (f), there appears a central peak, ∼0.25 arcsec from each outer peak and coincident with the stellar position. The axis joining all three peaks is aligned along a position angle (PA) of 140° ± 5°. This is consistent with values of 130°–160° previously reported in the literature from the optical through to near-IR (e.g. Pantin et al. 2000; Augereau et al. 2001; Grady et al. 2001; Ardila et al. 2007; Tatulli et al. 2011; Quanz et al. 2011; Avenhaus et al. 2014b), and in the submillimetre regime with ALMA (Pineda et al. 2014; Walsh et al. 2014). The relative brightness of the central peak compared to the NW and SE peaks is not well constrained, but again the NW side of the disc is brighter than the SE.

Also at ∼15 au resolution, but with a more circular beam, as in Figs 1(c), (e) and (f), another type of asymmetry appears in the disc. Especially in Fig. 1(c) and (f), the disc displays an almost horseshoe-shaped structure, with more emission in the SW than in the NE. The contrast between points on opposite sides of, and equidistant from, the stellar position is around a factor of 3, whilst even the horseshoe itself appears clumpy.

Finally, we note that the total flux measured in the 6 km array configuration on 2012 June 20 is 1–2 mJy less than that measured in compact hybrid configurations on 2007 October 4 and 2009 May 31 (see Table 1). This possibly indicates that there is a significant extended dust emission component which is filtered out by the interferometer for baselines longer than 80–100 m. This is supported by the 2008 June 27 track, where the flux on the shortest baseline of 31 m was significantly larger than would be extrapolated from a Gaussian fit to the flux on all other baselines (as determined from the annularly binned visibilities obtained with MIRIAD's UVAMP task).

3.3 Amplitude versus $u - v$ distance

The images themselves in Fig. 1 show that the gap radius in the HD100546 disc is ∼25 au, as judged from the separation between the emission peaks along the disc major axis. Another estimate can be obtained from the visibilities, as depicted in Fig. 2. This shows the real and imaginary parts as a function of deprojected $u - v$ distance from the disc centre, following the treatment of Hughes et al. (2007), and equivalently Berger & Segransan (2007). For the deprojection, we have used our own directly derived values for the major axis PA of 140° and the disc inclination from face-on of 40° (see the next section).

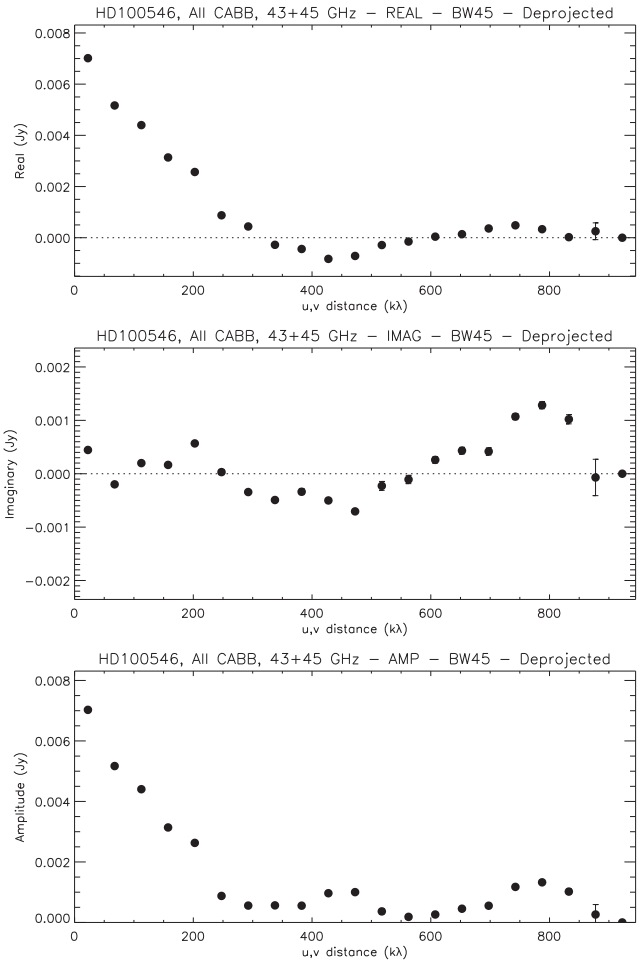

Figure 2. Real, imaginary and total visibility amplitudes versus deprojected $u - v$ distance computed using all the CABB data sets and combining both frequency sidebands. A bin width of 45 kλ has been used.

The plot shows a null in the real part of the visibility at 320 ± 10 kλ, determined using a linear fit to the binned visibilities in the region of ∼250–400 kλ. A similar feature has been observed in ten or so discs in recent years, and is indicative of a central hole or gap in the disc where there is a sharp change in the dust density (e.g. Hughes et al. 2007; Andrews et al. 2009, 2011a; Brown et al. 2009). Whilst all the CABB data has been used to construct Fig. 2 to enhance the S/N, the same null position is obtained – within the uncertainty range – separately for each frequency and each configuration with baselines sufficient to adequately sample the relevant $u - v$ space. Further, a similar value is found for 93.504 GHz data obtained in 2008 June (see Appendix A, Figs A1-b and A2, all only available online). On the other hand, recently published ALMA data at 0.9 mm by Walsh et al. (2014) instead show a null in the deprojected visibilities at 290 ± 5 kλ.

Using equation A11 in Hughes et al. (2007), the null at 320 kλ corresponds to a gap radius of 24.7 au, in good agreement with the value inferred from the reconstructed images. Equation A11 assumes that the emission occurs from a relatively thin ring of constant brightness, where the width of the ring is much less than

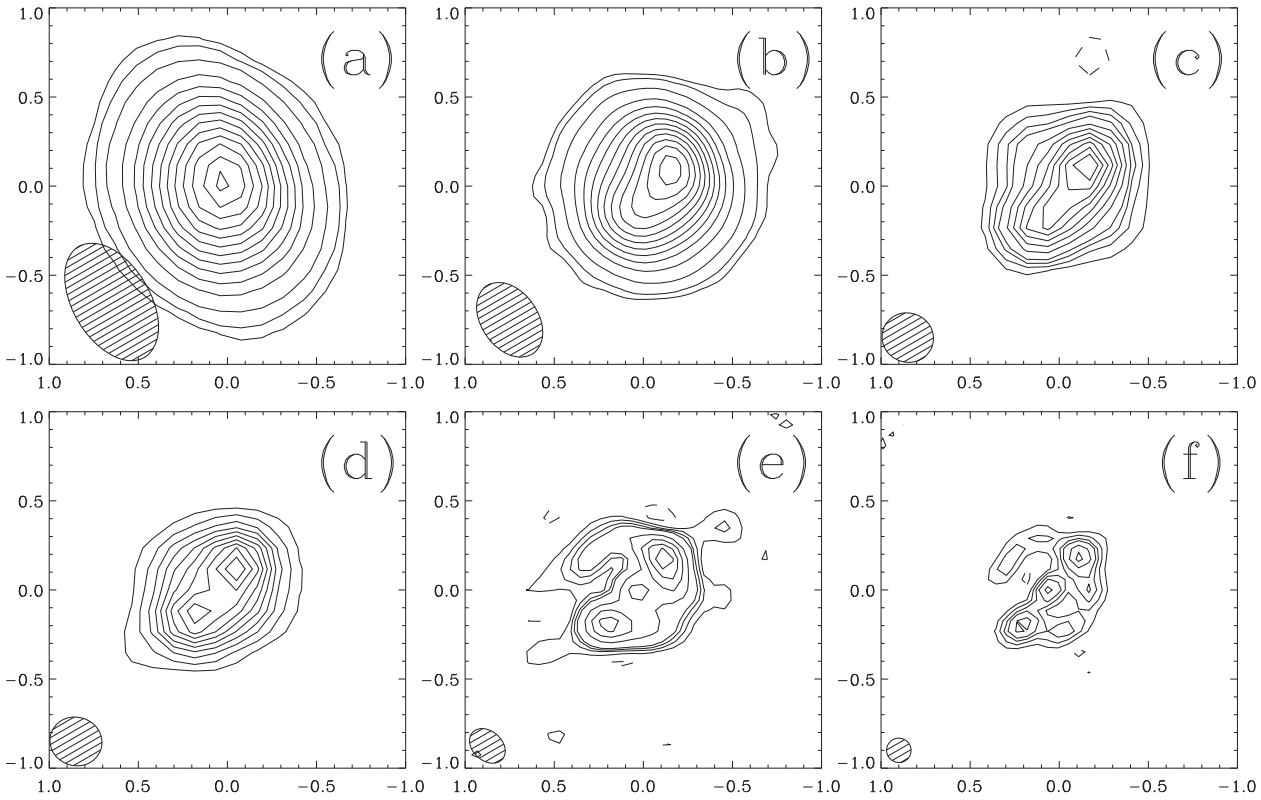

Figure 3. Self-calibrated images – phase only, two iterations – of HD100546 at 44 GHz using all the configurations for which CABB data was obtained. North is up and east to the left. The resolution increases from a–f, being: (a) 0.72 × 0.43 arcsec at PA = 30.°9 (natural weighting excluding antenna 6 baselines), with contours at 5, 10, 20, 40, 60, 80, 100, 120, 140, 160, 180, 200, 220, 235 times the rms of 0.0198 mJy beam^{-1}. (b) 0.46 × 0.32 arcsec at PA = 35.°1 (natural weighting including all baselines) with contours at 5, 10, 25, 50, 75, 100, 125, 150, 175, 200, 225, 250, 275 times the rms of 0.0119 mJy beam^{-1}. (c) 0.29 × 0.28 arcsec at PA = 68.°1 (superuniform weighting excluding antenna 6 baselines) with contours at 5, 10, 15, 20, 30, 40, 50, 60, 70, 80, 90 times the rms of 0.0273 mJy beam^{-1}. (d) 0.29 × 0.27 arcsec at PA = 73.°5 (superuniform weighting excluding antenna 6 baselines and 2012 June 20 data), with contours at 5–50 times the rms of 0.0402 mJy beam^{-1}, in steps of 5σ. (e) 0.23 × 0.16 arcsec at PA = 47.°9 (uniform weighting including all baselines) with contours at 5, 10, 15, 20, 40, 60, 80, 100 times the rms of 0.0180 mJy beam^{-1}. (f) 0.138 × 0.136 arcsec at PA = 62.°4 (superuniform weighting including all baselines) with contours at 5, 10, 15, 20, 30, 40 times the rms of 0.0359 mJy beam^{-1}.

its radius from the star, and the visibility function is a zeroth-order Bessel function. This may not necessarily be the case for HD100546. Equation A9 of Hughes et al. (2007) takes account of this, but requires knowledge of the sum of the power-law indices $p + q$ for the disc surface density and temperature radial gradients. Typical values of the surface density and temperature exponents are ∼1 and 0.5, respectively (e.g. d'Alessio et al. 1999). This would give a hole radius of ∼13.1 au, close to the value inferred from the optical, near-IR and mid-IR observations. Otherwise, a value of $p + q$ between 1 and 3 is reasonable (and required for Equation A9 to be valid) and gives radii of 11.5, 14.8 and 18.1 au for $p + q = 1$, 2 and 3, respectively.

In addition to the null at ∼320 kλ, a second and possibly third null are seen at between 550 and 600 kλ and ≤850 kλ, respectively. The existence of a second null is similar to the cases of SAO 206462, SR 21 and LkCa 15 in Andrews et al. (2011a,b). Assuming access to a telescope with even longer baselines (or equivalently the same telescope but with higher frequency receivers), we would expect this pattern of nulls to continue, as is the case for the circumbinary disc around the T Tauri system GG Tau in Guilloteau, Dutrey & Simon (1999). Such a 'ringing' pattern of the visibility amplitude in Fig. 2 is characteristic of a structure with relatively sharp boundaries between regions with and without emission.

3.4 Self-calibration

Although not shown in Fig. 1, signatures of phase errors, such as finger-like radial extensions, were seen in several tracks and in the combined data at levels of several times the rms noise. Their presence, along with the fact that we could be confident of having a good input model – given the extensive $u - v$ plane coverage of our data – motivated us to attempt self-calibration. The results are shown in Fig. 3.

Our procedure was to self-calibrate each frequency separately to serve as a consistency check. We also compared self-calibration results using the 'raw' 2048 × 1 MHz channel data averaged into 32 × 64 MHz channels (using MIRIAD's UVAVER routine). Solution intervals of 15 and 30 s were trialled. All combinations of input parameters produced results which were extremely consistent for the two sidebands. Further, two initial input models were tried, a clean component and a point source, and only two phase-only iterations were performed. Results were robust in the sense that the gross features in the final images were similar for the two initial models, though for the point source model the central peak dominates over the two others on either side.

The self-calibration produced images entirely consistent with those in Fig. 1, though with a much improved dynamic range, and showed similar behaviour as a function of $u - v$ plane coverage.

For instance, the presence or otherwise of a central peak within the inner disc gap is once again shown to be dependent on spatial resolution via the sampling and/or weighting of the visibility spacings. Also, the NW-SE brightness asymmetry is maintained, such that as the spatial resolution increases the NW side of the disc becomes prominent before the SE peak appears, and remains brighter at all scales.

Perhaps the best outcome from the self-calibration is that it 'sharpened' the image of the disc, in the process revealing part of the NE side of the disc in Figs 3e and 3f, which had only been hinted at in Fig. 1(c). However, the disc is still incomplete, being horseshoe-shaped with a large opening in its eastern side. Assuming the disc to be circular if viewed face-on, and fitting an ellipse to those images where the synthesized beam is close to circular, e.g. Figs 3(d) and (f), the disc inclination is estimated to be $40^\circ \pm 5^\circ$. This is consistent with values of 40°–50° previously reported in the literature from the optical through to near-IR (e.g. Pantin et al. 2000; Augereau et al. 2001; Grady et al. 2001; Ardila et al. 2007; Tatulli et al. 2011; Quanz et al. 2011; Avenhaus et al. 2014b), and in the submillimetre regime with ALMA (Pineda et al. 2014; Walsh et al. 2014).

4 DISCUSSION

Our observations present direct evidence at millimetre wavelengths for a ∼25 au radius cavity in the disc of HD100546, from the reconstructed images as well as the deprojected and binned visibilities. Although the ALMA submm observations of Walsh et al. (2014) and Pineda et al. (2014) also showed a null in the deprojected visibilities versus baseline, only Walsh et al. (2014) interpreted this in terms of a cavity within the disc. Neither author presented images showing the cavity, as their chosen antenna baseline weightings only gave spatial resolutions of ≤1 arcsec along the disc minor axis and 0.4–0.5 arcsec along the major axis. In this paper, we show that a resolution of better than about 0.3 arcsec is needed to see the cavity in reconstructed images. However, our images show not only the cavity, but also the existence of several asymmetries in the disc. We discuss each of these in turn below, as well as some of the inferred physical properties of the disc, such as its mass, overall size and dust population. Finally, we speculate on the type of planetary system that may be hosted by HD100546.

4.1 Cavity radius and variation with wavelength

Millimetre continuum observations trace the location principally of large dust grains, hundreds of microns to millimetre and even centimetres in size via their thermal emission within the disc mid-plane. On the other hand, the UV–optical–near-IR–mid-IR observations trace smaller dust grains, submicron to several microns in size, which scatter radiation off a disc 'atmosphere', and/or thermally emit from near a flared disc surface layer where they intercept direct stellar radiation. So it is perhaps not surprising that the two wavelength regimes typically produce somewhat different pictures of the disc, e.g. overall disc size (including the outer radius) and spiral patterns which have so far been difficult to (unambiguously) detect in the millimetre dust continuum.

But an interesting facet of our HD100546 data is that the radius of the inner disc gap – or perhaps more accurately the distance between the star and the peak of the 7 mm thermal dust emission – is around 25 au. This is significantly larger than the 14 ± 2 au radius inferred at much shorter UV-IR wavelengths, best seen in the surface brightness cuts of Avenhaus et al. (2014b) and Quanz et al. (2011). These display a clear maximum at ∼14 au, and certainly well short of 25 au. Our figure is extremely robust, being consistent amongst several different data sets.

This cavity size differential cannot be easily explained by the mid-plane versus surface/atmosphere locations of the respective dust populations, but it is a finding that is becoming increasingly common for other transition discs (e.g. Dong et al. 2012). Examples include SR 21 (Andrews et al. 2011a; Follette et al. 2013), MWC 758 (Andrews et al. 2011a; Grady et al. 2013) and SAO 206462 (HD135344B, Andrews et al. 2011a; Garufi et al. 2013). Further, in several cases including HD100546 (Brittain et al. 2009, 2013, 2014; Liskowsky et al. 2012), the atomic and/or molecular gas approaches closer to the central star. Other examples include J160421.7−213028 (Zhang et al. 2014) and those studied by Pontoppidan, Blake & Smette (2011) and Pontoppidan et al. (2008). Thus, the overall picture is one where the gas and small dust grains are well mixed and have a similar spatial distribution, but which is different for the large dust grains.

As well as the different cavity radius, the small dust grains and/or molecular gas in several transition discs (for which the respective data exists) also form a complete ring around the star, unlike the millimetre emission which only forms an arc or horseshoe (e.g. Oph IRS48 in van der Marel et al. 2013; HD142527 in Casassus et al. 2013 and Fukagawa et al. 2013). Both phenomena are well explained in a scenario where the large dust grains are caught (or trapped) at a pressure bump (Regaly et al. 2012; Pinilla, Benisty & Birnstiel 2012; Birnstiel, Dullemond & Pinilla 2013), across which the gas and small grains can diffuse.

Our inferred central cavity radius of the HD100546 disc of ∼25 au finds a parallel in the modelling of HD100546's disc by Mulders et al. (2013b). In order to reproduce mid-IR interferometric data these authors find that the boundary of the inner disc wall (near 13 au) cannot be sharp, but must instead be significantly rounded. The best-fitting radius they find – at which a steep drop-off of the disc surface density begins – is 29 au, with a range of 26–35 au. Similarly, modelling the disc as a ring with a Gaussian radial brightness distribution, Walsh et al. (2014) found that their ALMA 0.9 mm observations could be well fitted with a width of 21 au centred at 26 au.

In addition to the cavity size differential inferred from the large and small grain tracers, our 7 mm data also suggests a difference in gap radius inferred from long and short millimetre wavelengths. Specifically, the 7 mm visibility null determined here of 320 ± 10 kλ is significantly different to that measured at 0.9 mm by Walsh et al. (2014) of 290 ± 5 kλ. With a very fine coverage of the $u - v$ spacings the ALMA value is extremely well determined. Whilst our data does not have an equivalent 'fineness' in the $u - v$ coverage to determine the null position with the same level of precision, our S/N is still sufficient to have high confidence in our value. Thus, we are very confident that this is a real difference. To further check this, we have also used the same deprojection formula and values for the inclination and PA used by Walsh et al. This did reduce our null to 315 ± 10 kλ, but obviously still maintained the existence of the difference and approximately its magnitude as well. To our knowledge this difference is one of the first such findings for a transitional disc, and certainly the first across such a wide wavelength range of 1-to-7 mm. Recently van der Marel et al. (2015) found a similar effect for the first visibility nulls at 345 and 690 GHz for several transition discs, including HD135344B, SR 21 and RX J1615−3255, and also interpreted this as an increased cavity size at the longer wavelength.

The fact that the null at 7 mm is higher than at shorter millimetre wavelengths is in agreement with particle trapping theory induced by a massive planet, which predict different radial dust distributions for different grain sizes (Pinilla et al. 2012; de Juan Ovelar et al. 2013; Pinilla et al. 2014). According to these models, larger grains are expected to be more concentrated in the pressure maximum than smaller grains, implying a slight difference in the disc radial extension observed at 7 mm than at submm wavelengths. Thus, the larger particles to which our observing wavelength of 7 mm is biased are located slightly radially inwards of the smaller particles traced at 0.9 mm by the ALMA data. More detailed modelling of both the ALMA and ATCA visibilities, in the context of sequential planet formation in the disc, is presented in Pinilla, Birnstiel & Walsh (2015).

4.2 Disc size (outer radius)

From our best 7 mm data on 2012 June 20 the full width at half-maximum (FWHM) of the mm-emitting region is ∼50–60 au, from an elliptical Gaussian fit using MIRIAD's UVFIT. This is similar to the FWHM of ∼55 au found at 16 mm (also using UVFIT; Fig. A3 in Appendix A, only available online), and is little or no different to the outer radius at 0.87 mm of 40–60 au quoted by Pineda et al. (2014), or ≤100 au (and nearer ∼50 au) at 0.87–0.99 mm in Walsh et al. (2014). The visibilities at 3 mm presented in Fig. A2 also imply a very similar source size (see also Fig. A1-b). We have not used our other 3 mm data (Figure A1-a) to estimate a disc size due to the relevant data set having a poor phase correction. Perez et al. (2010) have shown how such an inadequate correction can lead to an unreliable estimate of the disc size.

Since each wavelength is most sensitive to emission from dust grains with size similar to that wavelength, then within the spatial resolutions achieved by the various above-mentioned data sets there is no evidence for a large-scale radial gradient in the 'characteristic' particle size (at least for millimetre-sized grains) within the HD100546 disc. As noted by Pineda et al. (2014), the outer radius of a dust disc should be the same when observed at different (sub)millimetre wavelengths for the case of a planet–disc interaction, while for pure radial drift the outer disc radius inferred from different wavelengths would be different (see also Birnstiel & Andrews 2014).

The 1–10 mm observations of the AS 209 and UZ Tau E discs presented in Perez et al. (2012) and Andrews (2013), respectively, demonstrate excellent examples where radial drift is likely to be occurring, and dominating the segregation of different particle sizes. Their visibility curves progressively broaden with increasing wavelength, indicating more and more compact emission for ever larger grains. For example, for AS 209 the FWHM of the deprojected and binned visibilities approximately doubles between 1–3 mm and 8–10 mm, whilst for UZ Tau E it increases by about a factor of 5. Assuming Gaussian source structures these represent concomitant changes in the size of the disc. This stands in contrast to the corresponding plots for HD100546, presented here at 3, 7 and 16 mm and at 1 mm in Walsh et al. (2014). All these have similar – though as alluded to above not necessarily precisely equal – widths, and thus provide yet more evidence of one or more planets already existing within the cavity of the HD100546 disc.

Of course, there is a large difference in the disc outer radius between the 1–16 mm observations and the UV–IR observations which are sensitive to much smaller sized grains. Similarly, the disc size measured in molecular gas tracers, such as CO (Panic et al. 2010; Walsh et al. 2014; Pineda et al. 2014) and HCO+ (Appendix B, only available online as supplementary material), is significantly larger than inferred from the mm-emitting dust. However, the data are insufficient to discriminate between scenarios where this contrast is due to radial migration of larger grains, which decouple more effectively from the gas, or whether the grains instead grew *in situ* within the inner disc. In the latter case, the dust density may be naturally higher, potentially providing a more conducive environment for grain growth. For instance, the dust density would increase radially inwards, so that the collision time-scale between grains would be shorter, and/or – as strongly suggested above – there could be local density enhancements arising from a pressure maximum, created within the inner disc via interaction with an orbiting body.

Interestingly, Quanz et al. (2011) present evidence from near-IR scattering data on 10–140 au scales that there may be a change in the relative fractions of large versus small grains at a disc radius of 40–50 au. Though only probing the surface layers of the disc, and still only sensitive to particles in the micron size range, that the larger ones dominate at radii encompassed by the total extent of the mm-emitting disc found here is suggestive of a relation between the two data sets.

4.3 NW–SE brightness asymmetry

The sense of the brightness asymmetry between the two sides of the disc at 7 mm is consistent with what is observed at 3 mm (Appendix A, Fig. A1-b, both only available online), but opposite to that found by Pineda et al. (2014) at 0.87 mm with ALMA. However, their result is based purely on the residuals of a model fit, in which the model assumes a fixed inner disc radius of 14 au, consistent with the value found from optical/near-IR scattering data, but less than the star-to-peak emission radius of ∼25 au found in the millimetre regime here and in Walsh et al. (2014). So our observed asymmetry is a more direct finding, and thus we believe more reliable.

Notably, the major axis brightness asymmetry we find is opposite to that seen in near-IR scattered light by Avenhaus et al. (2014b), who instead find the SE peak to be brightest, which they tentatively interpret as being due to it being closer to an orbiting companion. Also, from *Hubble Space Telescope* (*HST*) far-ultraviolet observations Grady et al. (2005) found that their inferred 13.0 ± 2.5 au radius cavity was not centred on the star, but instead ∼5 ± 3 au to the south-east along the major axis, where there was a local maximum in the reflection nebulosity, and implying an eccentricity of 0.38 ± 0.24. If the finding by Grady et al. is true then that would also mean the NW side of the disc is physically closer to the star. Thus, the dust on that side would be warmer leading to enhanced thermal emission, precisely what we observe.

But for this scenario to work – known as pericentre glow and also seen in the HR4796A debris disc (Wyatt et al. 1999; Telesco et al. 2000) – requires an elliptically orbiting body either inside or outside the disc. The elliptical orbit enforces an eccentricity to the orbits of dust particles, with the consequence that the inner rim of the disc also becomes elliptical, a prediction that finds support, in the case of HD100546, in the modelling of OH ro-vibrational spectra by Liskowsky et al. (2012) and the direct observation of Grady et al.

Also, for HD100546 the Grady et al. observation would predict the orbiting body's apocentre, i.e. its furthest distance from the star, to be on the SE side of the disc. For an elliptical orbit the apocentre is also the direction in which the body spends most of its time, since its velocity is lower than when it approaches close to the star. Thus, from a statistical perspective, for any one system we would expect to find an orbiting body closer to its apocentre than its pericentre. In the timeframe of our observations, this does appear to be the

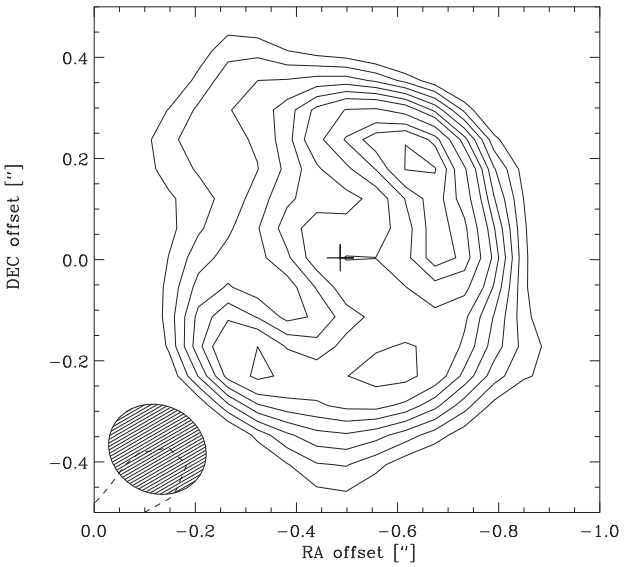

Figure 4. Reconstructed image at 44 GHz from 20 June 2012, using uniform weighting and contour levels at 5, 7, 9, 11, 13, 15, 18, 21, 23, 25.7 times the RMS of 0.03034 mJy beam^{-1}. Synthesized beam is 0.20 arcsec × 0.18 arcsec at PA = 74.5°. A colour version of this image is available in the online-only supplementary material (Appendix A, Fig. A4).

case for HD100546, at least for the postulated inner body (Brittain et al. 2013, 2014). Further, it is probably this body that would most influence the inner regions of the disc due to both its relative proximity (10–15 au compared to 50–70 au for the outer body) and its so far higher estimated mass range (Mulders et al. 2013b, Quanz et al. 2013a).

Whilst we propose here that an elliptically orbiting planet imposes the eccentricity on to the disc, this is not actually necessary. The hydrodynamic simulations of Kley & Dirksen (2006) and Ataiee et al. (2013) show that a $\geq 3\,M_J$ planet in a circular orbit around a solar mass star can also induce a significant eccentricity on the disc, e.g. up to $e = 0.25$, via an instability. But given that 3 of the 4 gas giants in our Solar system have an eccentricity of ∼0.05, and that the distribution of extrasolar planet eccentricities peaks between $e = 0.1$ and 0.4 (Wright et al. 2011), then it is reasonable to presume that these 'end state' planet orbits are a reflection of the situation in their precursor disc stage. Though obviously there could be orbital evolution of any one particular planet, it seems credible to anticipate that any planet(s) around HD100546 could also be in an eccentric orbit.

Our best data set, that of 2012 June, provides direct support for the 'pericentre glow' scenario, and thus very strongly supports the existence of one or more inner orbiting bodies. Fig. 4 – also available in colour online in Appendix A – shows an expanded view of the 44 GHz image in Fig. 1. The cross marks the position of the star after accounting for its proper motion of -38.93 ± 0.36 mas yr^{-1} and 0.29 ± 0.38 mas yr^{-1} in RA and declination (van Leeuwen 2007) from its J2000 position over a 12.5 yr period. Whilst the NW and SE peaks are aligned along a similar axis through the stellar position, the NW peak is slightly closer to the star. The individual 43 and 45 GHz images show a consistent trait. The implied eccentricity is only about 0.06, less than that implied by the Grady et al. (2005) result of 0.38 ± 0.24 or the lower limit of Liskowsky et al. (2012) of ≥0.18 (0.07–0.30 at 99.7 per cent confidence). However, these latter two estimates are for smaller disc radii, ∼13 au, whilst ours is for further out in the disc at ∼25 au. Assuming a $1/r^2$ falloff in the eccentricity (Liskowsky et al. 2012 and references therein) the expected value at 25 au is ≥0.05, or 0.11 ± 0.05, figures much more in line with our determination.

Finally, we point out that the 3.81 μm NACO/VLT (NAOS-CONICA/Very Large Telescope) sparse aperture masking (SAM) images of HD100546 presented in Marino et al. (2014a,b) also suggest that the ∼13 au radius cavity (at this wavelength) around HD100546 is eccentric. As at 7 mm here, the SAM data detect both the star and the disc in the same image, which shows a slight but distinct offset of the star north-west from the centre of an elliptical ring, and along its major axis. This is similar to the sense observed by Grady et al. (2005), but the magnitude of e of ∼0.15 is less than half their best estimate, though within the uncertainty range and close to the value of 0.18 from Liskowsky et al. (2012). In the interest of completeness we note that, from near-IR polarimetric differential imaging, Avenhaus et al. (2014b) exclude an eccentricity of ≥0.133 at 99.8 per cent confidence for their 14 ± 2 au radius inner disc rim.

4.4 NE–SW azimuthal asymmetry

In addition to the major axis asymmetry discussed above, there is also a minor axis asymmetry apparent in our 7 mm images. Such an azimuthal asymmetry, in the shape of an arc or horseshoe, has been found in the millimetre regime around several Herbig stars with transition discs. The factor of about 3 contrast for HD100546 is not nearly as dramatic as values of ≥130 for Oph IRS48 (van der Marel et al. 2013) or 30 for HD142527 (Casassus et al. 2013; Fukagawa et al. 2013), but is similar to those for other transition discs like LkH α 330 (Isella et al. 2013) and SR 21 and SAO 206462 (HD135344B; Perez et al. 2014). These asymmetries, typically interpreted recently in the context of a pressure bump/dust trap model mentioned above, may well be the result of on-going planet formation in the discs (e.g. Ataiee et al. 2013; Birnstiel et al. 2013; Fu et al. 2014).

Interestingly, the arc of millimetre emission in HD100546 is on the same side as a 'dark lane' seen in scattered light in the H and K bands by Avenhaus et al. (2014b). As Figs 3 and 4 in Avenhaus et al. (2014b) show, the dark lane begins at about 20 au from the star, similar to the millimetre emission, but its radial extent is apparently larger. Taken together, the bright millimetre thermal emission but faint near-IR scattered light is consistent with the SW being the near side of the disc, as also inferred by other authors (e.g. Quanz et al. 2011, and references therein). In other words, the dense, mid-plane of the disc closer to Earth shadows and obscures part of the far side.

As further support for this non-axisymmetry seen in the image plane, if the HD100546 disc was instead axisymmetric then with a suitable choice of the disc inclination and major axis PA the de-projected imaginary component of the visibilities should be close to zero. This is clearly not the case in Fig. 2, and no other choice of inclination and PA (consistent with literature values) makes it so. Thus, as the reconstructed images in Fig. 1 suggest, the structure in the imaginary component is proof that the HD100546 disc is not axisymmetric at 7 mm. This is similar to the case of the LkHα 330 disc at 1 mm in Isella et al. (2013). Leveraging off their work, from Fig. 2 the imaginary component appears to oscillate around zero with an amplitude of around 1 mJy at ≥200 kλ. Assuming a total integrated flux of around 7 mJy for the compact disc (2012 June 20 data in Table 1) this implies that only about 15 per cent is contributed by the asymmetric part of the disc. Such an implied 'average' contrast is notably higher than the point-to-point

brightness contrast of ∼3 for the azimuthal asymmetry inferred from the reconstructed images.

The imaginary component in Fig. 2 approximates to zero at baselines less than about 200 kλ. This is even more obvious when narrower bin widths are used. It may suggest that the disc is axisymmetric on large spatial scales. This appears to be supported by the ALMA 300–350 GHz data of Walsh et al. (2014), where they find the imaginary component to be zero up to a baseline of 300–350 kλ, at which point it rapidly increases above zero. Their $u - v$ coverage cuts off at ∼400 kλ so a more complete comparison with our data cannot be made. We do however note that, whilst the respective data sets are qualitatively similar, where the imaginary component in our data first goes negative, in Walsh et al. it first goes positive. This does not appear to be due to the different deprojection formulae, of which we have used those in Hughes et al. (2007) and Walsh et al. used those in Berger & Segransan (2007).

Interestingly, from mid-IR interferometry Panic et al. (2014) find a significant deviation of their phases from zero, from which they infer an asymmetry in the disc wall at ≥10 au from the star. They did not state the azimuthal position of the asymmetry, but since the bulk of their baselines were closer to the PA of the disc minor axis suggests that the asymmetry is approximately along that axis as well. A departure from centrosymmetry is also inferred by Lazareff et al. (2013) from near-IR interferometric data obtained with the PIONIER instrument. Finally, the reconstructed images from the 3.8 μm SAM observations of Marino et al. (2014a,b), also appear to show a horseshoe-like region, in which there is significantly more emission to the SW than NE at radii of 10–15 au.

Thus, three separate near- to mid-IR data sets suggest that the HD100546 disc is asymmetric, and probably in the same sense as inferred from our millimetre observations. If true this would imply similarly asymmetric distributions of the small and large dust grain populations, albeit at radii of ∼12 and 25 au, respectively. It remains to be seen whether such a scenario is consistent with the pressure bump/dust trap model, which typically implies that the smaller grains can diffuse through the trap, along with the gas. This does appear to be the case radially for HD100546, but apparently not azimuthally. Alternatively, it is perhaps as simple as the fact that the dust trap is a reservoir of material, in which the fragmentation products of collisions between large particles naturally lead to similar azimuthal spatial distributions for small and big dust grains.

4.5 SED and dust grain size

Using total fluxes of 1110 ± 180 mJy (Walsh et al. 2014), 560 ± 140 mJy (Henning et al. 1994, 1998), 45 ± 5 mJy (Table A1, only available online) and 8.5 ± 0.5 mJy (Table 1), at, respectively, 'effective' frequencies of 324, 236, 90 and 44 GHz, the best-fitting spectral index α to the SED is ∼2.45 ± 0.08 (formal fit error). This is shown in Fig. 5, where the entire SED from ∼1 to 60 mm is presented. The 3 mm, 16 mm, 3.5 cm and 6.2 cm data are presented in Appendix A and discussed in Appendix C (both only available online), where respective contributions from thermal dust and free–free emission are discussed.

With a spectral index from 0.9 to 7 mm of ∼2.45, and assuming optically thin emission, the dust emissivity index β, where $\kappa \propto \nu^{\beta}$, is ∼0.45. A rough correction to this value can be made where there is some contribution from optically thick emission, which tends to increase β. From independent samples of T Tauri stars both Rodmann et al. (2006) and Lommen et al. (2007) inferred values of δ, the ratio of optically thick to thin emission, of around 0.2. Using the relation $\beta_c = (\alpha - 2)(1 + \delta)$, we therefore find the corrected value

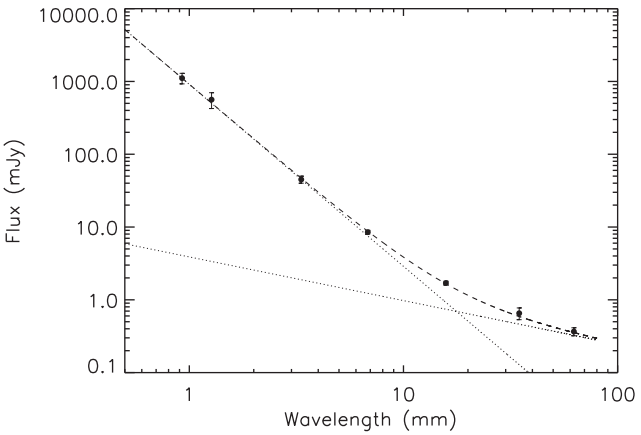

Figure 5. SED of HD100546 from ∼1–60 mm. Total 'average' fluxes at 16 mm, 3.5 cm and 6.2 cm are 1.7 ± 0.1, 0.65 ± 0.12 and 0.37 ± 0.05 mJy, obtained from the tables in Appendix A (only available online). The dashed line is a composite 'fit' to the SED assuming thermal dust emission with slope 2.45 ± 0.05 dominates at 1 to 16 mm and free–free with spectral index 0.60 ± 0.05 dominates at 3.5 to 6.2 cm (both represented by dotted lines). The two respective contributions are 'anchored' at 3 mm with a flux of 45 ± 5 mJy and at 6.2 cm with a flux of 0.325 ± 0.025 mJy. See Appendix C for further details, available online only.

to be $\beta_c \simeq 0.54$. Since our 16 mm flux, which is spatially resolved, also falls nicely on a fitted SED slope of 2.45 – after accounting for a free–free emission component (see Appendix C, only available online) – the case for invoking an optically thick component is weakened. We also note the work here of Ricci et al. (2012). Thus, in the following we will assume a value of $\beta = 0.5 \pm 0.1$.

Such a relatively low value for β suggests that the dust grains in the HD100546 disc have undergone significant growth from their original interstellar medium (ISM) submicron sizes, where β is typically around 1.7 (Draine 2006). As noted by van der Marel et al. (2013), dust grains larger than ∼three times the observing wavelength do not contribute to the opacity. Thus our 7 mm data suggests growth up to at least 2 cm. But given we have also detected dominant thermal dust emission at 16 mm, and probably a significant dust emission component up to 3.5 and even 6.2 cm (Fig. 5 and online-only Appendix C), then we can say with high confidence that growth has occurred up to at least 5 cm and probably up to around 20 cm.

We can potentially improve upon these rough estimates by appealing to cosmic dust models. Using the astrosilicate curve in fig. 6 of Draine (2006) our value for β can only be compatible with a grain size distribution $dn/da \propto a^{-p}$ for p around 3.2 and maximum size a of 100 cm. A similar inference can be made from the porous icy grain model in Testi et al. (2014), composed of astronomical silicates, carbonaceous material and water ice, with relative abundances as in Pollack et al. (1994) and a porosity of 50. And similarly for the compact, segregated spheres model of Natta et al. (2004, 2007). In these cases, the maximum grain size is again ≥100 cm for $p \leq 3.3$, or about 10 cm for $p = 2.5$.

Interestingly, no grain model considered above can produce a β less than about 0.5, regardless of maximum grain size, unless the index p in the grain size distribution is ≤3. This suggests that the dominant process governing the grain size distribution in the millimetre-emitting HD100546 disc is not one of fragmentation and shattering, as might be expected in a collisionally evolved disc (or the ISM where $p = 3.5$). Instead, an index $p \leq 3$ is expected for the case in which coagulation and growth determines the size

distribution (e.g. Natta & Testi 2004; Birnstiel et al. 2010; Pinilla et al. 2014 and references therein). On the other hand, as noted by Dullemond & Dominik (2005) this growth process itself does maintain a population of small grains – via shattering collisions – which would otherwise be lost to the system on a time-scale much shorter than its few-to-several Myr age. The signature of these grains is at much shorter wavelengths, namely optical/near-IR scattering and mid-IR thermal emission. Indeed, from radiative transfer modelling where p was a free parameter, Harker et al. (2005) found a best-fitting value of $p = 3.5$ for the SED up to 100 μm.

The fact that grains as large as several tens of centimetres exist at radii out to a few tens of au is a specific prediction of the dust trap models previously mentioned. Given the age of the HD100546 system is a few to several million years, under the ordinary radial drift scenario such grains would have long ago spiralled into the star – the so-called 'metre-size barrier'. A long-lived mechanism must therefore be acting to keep such particles out there, and, given the size distribution index is $\leq$3, allow their growth to be ongoing.

Finally, from models that combined hydrodynamical simulations with dust evolution of a planet-sculpted cavity, Pinilla et al. (2014) found a linear relation between the disc integrated 1–3 mm spectral index and the cavity radius for transitional discs with a dust trap. The correlation is such that the millimetre SED slope $\alpha_{1-3\,\mathrm{mm}}$ increases with cavity radius, and provides reasonable agreement with the observed properties of 20 transition discs. It results from the fact that for discs where the pressure bump is located further from the star (i.e. wider cavities), the maximum and critical grain sizes – where the latter is the particle size that is perfectly trapped by the pressure bump – are expected to be smaller. The correlation is $\alpha_{1-3\,\mathrm{mm}} = 0.012 \times R_{\mathrm{cavity}} + 2.15$, which, using the mm-inferred cavity radius of 25 au for HD100546, predicts a spectral index of 2.45, in precise agreement with the value reported here.

4.6 Disc mass and inferred gas-to-dust mass ratio

The dust mass in the disc can be obtained from the deceptively simple equation $M_{\mathrm{dust}} = (F_\nu d^2)/(B_\nu(T_\mathrm{d})\kappa_\nu)$, where F_ν is the observed flux at frequency ν, d is the distance, $B_\nu(T_\mathrm{d})$ is the Planck function at the dust temperature T_d and κ_ν is the dust opacity. Whilst the distance and flux are well known, the derived mass can be poorly estimated due to inadequate knowledge of the dust temperature and most especially the dust opacity κ. In addition to composition, the latter has a strong dependence on grain size, decreasing as the size increases (e.g. Miyake & Nakagawa 1993). So an overestimate of κ, e.g. by using a value for small grains for a disc with ostensibly large grains, would seriously underestimate the dust mass of the disc.

Therefore, we use a range of κ values at 7 mm for amorphous silicate spheres from Draine (2006) to give a sense of the uncertainties involved. These are 0.2, 0.09 and 0.03 $\mathrm{cm^2\ g^{-1}}$, appropriate for a grain size distribution with an index of $p = 3.5$, minimum grain size a_{min} of 3.5 Å, and maximum size a_{max} of 1, 10 and 100 cm, respectively. These give dust masses of ∼0.33, 0.73 and 2.2 M_J, respectively, assuming a temperature of 40 K. A temperature variation of ± 20 K changes these estimates by factors of ∼0.7 for 60 K and ∼2.0 for 20 K. Similar masses are obtained using the opacities for the grain compositions, structures and sizes given in Natta & Testi (2004), and in this case account can be taken of a lower size distribution index p.

If a relatively flat grain size distribution exists in the disc around HD100546, as discussed above, then it means that relatively more mass is contained within larger particles. The opacity κ could therefore be even lower than assumed above, and the derived masses subsequently increase. Notably, these masses are at least an order of magnitude larger than the estimate of Walsh et al. (2014) from ALMA 1 mm data, who used both a higher κ and higher β.

Panic et al. (2010) observed various rotational transitions of CO in the HD100546 disc and estimated a mass of $\sim 10^{-3}$–$10^{-2}\ \mathrm{M_\odot}$, or 1–10 M_J, of molecular gas within a radius of approximately 400 au from the star. Without even accounting for the factor ∼8 difference in the disc outer radii of the molecular and millimetre continuum emission, there is a clear indication in the ATCA data that the gas-to-dust mass ratio in the HD100546 disc has decreased from its canonical value of ∼100 in the ISM and molecular clouds. Unless a significant amount of material is hidden from view because it is in bodies much larger than a metre or so in size, there is apparently little material available for further gas-giant planet building within the HD100546 disc. We refer to Bruderer et al. (2012) for a detailed discussion of the gas-to-dust mass ratio towards HD100546.

4.7 Nature of the central emission peak

Our observations have revealed a local maximum in emission at the position of the central star, with a similar flux level as that from the two peaks on either side along the disc major axis (Figs 1 and 3). Isella et al. (2014) also found a central emission peak at 7 mm for the transition disc source LkHα 15. An obvious question to be posed concerns the physical mechanism behind the emission, options being the stellar photosphere, hot dust from an inner disc, free–free from a wind or some thermal shock, accretion or other non-thermal process where material is accreting on to the star. All these have an observational basis for being tested, since an inner dust disc was found by Panic et al. (2014), and both outflow and accretion signatures have been detected via various phenomena (e.g. Vieira et al. 1999; Deleuil et al. 2004; Grady et al. 2005; Guimaraes et al. 2006). Indeed, our own radio observations, combined with IR recombination line data and discussed in Appendix C in online-only supplementary material, suggest an outflow rate of $\geq 10^{-8}\ \mathrm{M_\odot\ yr^{-1}}$.

All of these processes probably contribute at some level. The inner dust disc from Panic et al. (2014) only extends to a maximum radius of ∼0.7 au and probably even smaller, of the order of ∼0.3 au (Mulders et al. 2013b). The total mass of dust in this disc was not estimated by these authors, but Benisty et al. (2010) infer it to be only $\sim 3 \times 10^{-7}\ M_\mathrm{J}$ composed of only 0.1–5 μm sized grains. Also, its temperature would obviously be in the range of hundreds up to even a thousand Kelvin, much hotter than the colder and more massive disc responsible for the bulk of the millimetre emission. It thus seems reasonable to conclude that the lower dust mass, smaller grain size and higher dust temperature would all conspire to produce much less 7 mm emission than is observed for the central peak, especially given the latter's comparable flux level to those of the major axis peaks of the outer disc.

We instead assess that the central emission seen at 7 mm arises from free–free emission from an outflowing wind. The radio emission we found at 4.8 and 8.64 GHz has a spectral index very close to the canonical value of ∼0.6 for a spherical wind (online-only Appendix C; Panagia & Felli 1975). Further, the fluxes themselves suggest that up to about 10 per cent of the total emission at 7 mm could originate from this wind. This implies that the central peak would have a flux of around 1 mJy, which seems consistent with our observations.

Finally, we can almost certainly rule out thermal shock and/or accretion emission since, as noted by Skinner, Brown & Stewart (1993) in their radio continuum survey of Herbig Ae/Be stars, the

Table 2. Summary of D'Alessio models that can fit the HD100546 mm to cm emission.

$T_{\rm eff}$ (K)	Age (Myr)	Mass ($M_\odot$)	Luminosity ($L_\odot$)	$\dot{M}$ ($M_\odot$ yr^{-1})	$R_{\rm in}$ (au)	$R_{\rm out}$ (au)	p	$a_{\rm max}$ (cm)	$M_{\rm dust}$ (M_J)
				Disc mid-plane					
10^4	1	4.0	251.9	10^{-7}	1.34	300	2.5	10	4.3
10^4	10	2.3	29.5	10^{-7}	0.48	300	2.5	10	5.7
9×10^3	1	4.0	210.0	10^{-7}	1.24	300	2.5	10	4.6
9×10^3	3	2.7	71.0	10^{-7}	0.72	300	2.5	10	5.1
9×10^3	10	2.0	17.1	10^{-7}	0.38	300	2.5	10	6.0
8×10^3	1	4.0	165.1	10^{-7}	1.09	300	2.5	10	5.1
7×10^3	1	4.0	130.4	10^{-7}	0.97	300	2.5	10	5.4
6×10^3	1	3.5	59.1	10^{-7}	0.65	300	2.5	10	6.1
5×10^3	1	3.0	14.9	10^{-7}	0.34	300	2.5	10	7.1
5×10^3	1	3.0	14.9	10^{-7}	0.34	100	2.5	10	2.7

expected spectral index is −0.1. This is much different to the index found at 4.8–8.64 GHz. Also, based on the formulae given in Skinner et al. and using our own plus literature values for accretion and/or wind mass-loss rates for HD100546, the expected 4.8–8.64 GHz fluxes are far above what was measured. See Appendix C for further details, available online as supplementary material.

4.8 Modelling the large grain population

Several seemingly quite successful attempts have been made to model the HD100546 SED with radiative transfer calculations up to 1–3 mm, assuming a disc extending from about 10 to 400–500 au. For instance, using similar data sets Benisty et al. (2010) and Tatulli et al. (2011) find a disc dust mass of around 0.5 M_J for a grain size distribution between 1 μm and 1 cm ($p = 3.5$). Bouwman et al. (2003) and Doering (2008) instead find an order of magnitude lower mass, around 0.065 M_J, with the former using grain sizes of 10–200 μm ($p = 2$) and the latter 0.01 μm–1 cm ($p = 3.5$).

As noted by Espaillat et al. (2010), the largest uncertainty in any model is in the adopted mass opacity of the dust. In the case of HD100546 those models with the least mass in larger grains, and thus opacities which are too high, severely underestimate the disc mass calculated from the observed fluxes, yet can still produce a reasonable match to the SED up to 1 mm. But even so, in all cases where the model extends to 3 mm the flux is underpredicted. It is anticipated that if these models were extended out to 7 and 16 mm they would increasingly fail to predict the observed flux, necessitating such data as presented here.

Since none of the models were optimized to fit the long wavelength data, i.e. at ≥3 mm, none attempted to assess the large grain population. Although we believe our data is sufficiently unique to stand on its merits, we have attempted to model the mm–cm fluxes using the irradiated accretion disc models of D'Alessio et al. (2005). These models do not consider the disc to be simply reprocessing stellar radiation, but also to be self-luminous through an accretion flow. A comprehensive model grid is available for download from the web,[3] covering a large range of parameter space which overlaps with those inferred from our data, such as the maximum grain size, power-law size distribution, and the accretion rate. Further, proper stellar atmosphere (Kurucz) models are used as input, rather than the assumption of a blackbody.

[3] https://www.cfa.harvard.edu/youngstars/dalessio/

The D'Alessio models have been used to successfully model the SED of Herbig Ae/Be stars. For example, Merin et al. (2004) produced a good fit to the SEDs of HD34282 and HD141569, both of which overlap in properties to HD100546. We follow the approach they used for HD34282, and instead of trying to match the entire SED only consider the disc mid-plane component, responsible for much or all of the millimetre to centimetre emission. We consider the data from 0.9 mm all the way up to 6 cm, corrected for free–free emission (see Appendix C for details of the correction, available online as supplementary material).

Some of the free parameters can be fixed or constrained to a narrow range given what is known about HD100546, e.g. the distance is fixed at 100 pc. A range of stellar effective temperatures and ages bracket the ∼2.4–2.8 $M_\odot$ mass and 30–100 $L_\odot$ luminosity of HD100546 reported in the literature (e.g. van den Ancker et al. 1997; Blondel & Djie 2006), or even the figures of 4 ± 1 $M_\odot$ and $\log(L/L_\odot) = 2.65 \pm 0.25$ of Levenhagen & Leister (2004). So we have examined models with $T_{\rm eff}$ from 5000–10 000 K and ages 1–10 Myr. The HD100546 disc inclination is 40°–50°, between the two values of 30° and 60° offered in the grid, but which anyway had little effect on the fluxes and no detectable influence on the mm–cm SED slope. The outer radius is fixed to be 300 au for the 6000–10 000 K cases, closest to the observed radius of the millimetre-emitting disc of HD100546 of ≤100 au, whilst the 5000 K model does have a 100 au radius option.

We stress here that we are not claiming that $T_{\rm eff}$ for HD100546 is as low as 5000–8000 K. As a late B star, it is certainly higher, up to 10 500 K (van den Ancker et al. 1997) or even 11 000–12 000 K (Acke & Waelkens 2004; Levenhagen & Leister 2004), but those model grids are not available in the d'Alessio web archive. Rather, our aim here is simply to show that the long wavelength SED fluxes and slope are essentially independent of the stellar properties, through effective temperature and mass, but instead principally determined by, respectively, the luminosity (stellar plus accretion) and grain opacity (and thus disc mass).

Indeed, experience showed that the main input parameters in the models which affected the SED were the mass accretion rate $\dot{M}$, the maximum grain size $a_{\rm max}$ and the index p of the power-law grain size distribution. Available in the grid were four values of $\dot{M}$ from $\dot{M} = 10^{-9}$ to 10^{-6} $M_\odot$ yr^{-1}, six values of $a_{\rm max}$ from 1 μm to 10 cm, and two values of p, 2.5 and 3.5 representing dominant growth and fragmentation processes, respectively. We considered variations of these parameters for multiple combinations of the stellar properties, shown in Table 2, which also summarizes the

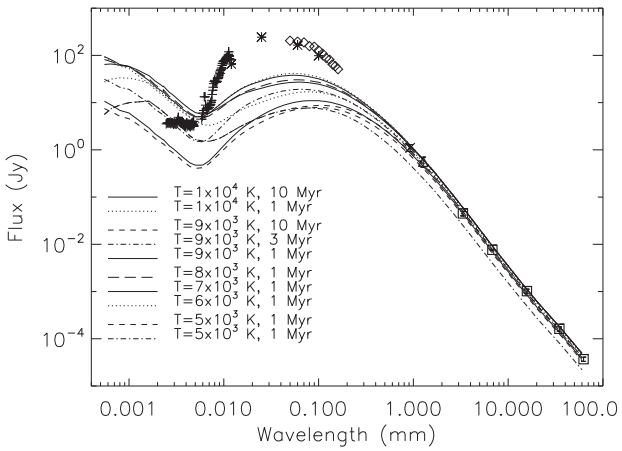

Figure 6. SED of HD100546 from the near-infrared to centimetre regime, with fits to the disc mid-plane emission from the D'Alessio irradiated accretion disc model as listed in Table 2. The 2.5–11.5 μm (plus signs) and 50–200 μm (diamonds) data are, respectively, from ISOPHOT and ISO-LWS (binned in 10 μm intervals) taken from the ISO Data Archive. Other points (asterisks) are the *IRAS* 12, 25, 60 and 100 μm fluxes. The ALMA 900 μm flux (cross) is from Pineda et al. (2014) and Walsh et al. (2014), whilst the SEST flux (triangle) is the mean of the two values reported by Henning et al. (1994, 1998). ATCA data reported here are shown as squares, corrected for free–free emission.

parameter combinations that could reasonably fit the mm-to-cm spectrum (see Fig. 6).

We found that no combination of stellar properties with an $\dot{M}$ of 10^{-6} or 10^{-9} $M_\odot$ yr^{-1} could match the observed fluxes. The former produced far too much emission whilst the latter provided far too little. An $\dot{M} = 10^{-7}$ $M_\odot$ yr^{-1}, along with $a_{\rm max} = 10$ cm and index $p = 2.5$ provided by far the best match to the data. If $a_{\rm max}$ was reduced to 1 cm then an accretion rate of $\dot{M} = 10^{-8}$ $M_\odot$ yr^{-1} could almost fit the fluxes up to 3 cm, but bigger grains are needed for the 6 cm data point. For $p = 3.5$ with $a_{\rm max}$ of either 1 or 10 cm the spectral slope was clearly too steep. The models definitely needed more of the available mass in the bigger grains (or equivalently less in the small grains and thus less emissivity at shorter wavelengths).

Fig. 6 shows the models from Table 2. We have chosen not to include shorter wavelengths (UV, optical, near-IR) as that part of the SED has been adequately treated elsewhere (e.g. Malfait, Bogaert & Waelkens 1998a; Mulders et al. 2011), and our intention is to instead treat the mm–cm component which has not been addressed in detail before. As previously noted, and now demonstrated in Fig. 6, the fits in the mm–cm regime are insensitive to the stellar properties ($T_{\rm eff}$, mass), and instead are particularly sensitive to the dust mass in the disc via the relative proportions of small and large particles. The average mass of around 5 $M_{\rm J}$ for the 300 au radius discs compares favourably with our observationally derived value of ∼1 $M_{\rm J}$ discussed previously. The only model in Fig. 6 which does not fit the fluxes – but still reproduces the slope – is for a disc radius of 100 au, and thus a factor of two lower dust mass.

As well as those papers cited above, other authors have optimized their radiative transfer models to fit shorter wavelength data, i.e. up to only a few hundred microns, and especially to constrain the dust mineralogy (e.g. Malfait et al. 1998a; Dominik et al. 2003; Elia et al. 2004; Harker et al. 2005; Mulders et al. 2011). Using the D'Alessio irradiated accretion disc prescription, we were unable to find a model to fit the predominantly surface layer origin near-, mid- and far-infrared emission of HD100546 that was physically consistent with the millimetre–centimetre model. This is apart from a general result that it almost certainly requires a separate population of much smaller grains, with a maximum size between 1 and 10 μm, in agreement with the aforementioned earlier studies.

But given the differences between some of the (fixed) model parameters and real properties of the disc, the inability to find a physically consistent model is not surprising. For example, the model and observed 1–16 mm disc outer radii differ by a factor of around 3. Most crucially the model assumes the disc extends all the way in to the dust sublimation radius, typically ≤1 au, whereas there is a ≥10 au wide gap between the compact inner disc of HD100546 (which generates the near-IR emission) and the extended outer disc (the inner wall of which produces most of the mid-IR emission). Though not completely cleared of gas and dust, the much reduced density in the gap will obviously result in significantly less emission than the models would otherwise predict.

These apparently have a secondary effect on the mm–cm SED. Indeed, it is impressive that the d'Alessio models do so well in fitting the HD100546 mm–cm data. Presumably the emission from the colder outer disc and its mid-plane has little 'memory' of the region (e.g. its density and temperature structure) in which original stellar and accretion ultraviolet radiation is processed into infrared radiation which eventually heats the dense disc interior. In conclusion, we find that the D'Alessio models can reproduce the mm–cm SED of the HD100546 disc with a set of parameters, specifically $\dot{M}$, p and $a_{\rm max}$, which had previously been inferred directly from the data.

4.9 Conjecture on the type of planetary system hosted by HD100546

4.9.1 General review of exoplanet statistics

As some indication of what may be expected of the planetary make-up of transition disc systems, we can look to the statistics of confirmed exoplanets and/or brown dwarf companions around solar analogues. Though a generalization, the logic behind this is simply that the end result of planet formation should at least partly be a reflection of what occurred during the formation phase, though of course keeping in mind the possibility of perturbing processes such as scattering and migration during the intervening period.

There are now a sufficient number of confirmed exoplanets, with well-defined properties, that we can begin to speculate on what the planetary system of their evolutionary precursors could (or should) look like. For this purpose, we use as one resource the Exoplanet Orbit Database (EOD) of Wright et al. (2011), which includes bodies up to 24 $M_{\rm J}$. Further, numerous massive exoplanet and/or brown dwarf companion direct imaging surveys towards Sun-like stars have been of sufficient sensitivity that statistical estimates can be made for the frequency of such bodies at various orbital radii.

At the time of writing there are just over 1500 confirmed exoplanets in the EOD, discovered primarily using transit and radial velocity (RV) techniques, but also including a few tens from direct imaging. These have their own – in many cases different – sensitivities to planets of different masses at various orbital radii (or equivalently orbital periods), and thus there is a risk of succumbing to selection bias when extracting statistical data. Whilst taking on board the specific caution of Wright et al. in this regard, here we only infer gross properties and check their robustness against the different discovery techniques, the specific biases of which can partially compensate each other.

With the caveat that only a handful of confirmed exoplanets orbit host stars with mass ≥2 $M_\odot$, the $\log_{10}$(Mass) distribution of

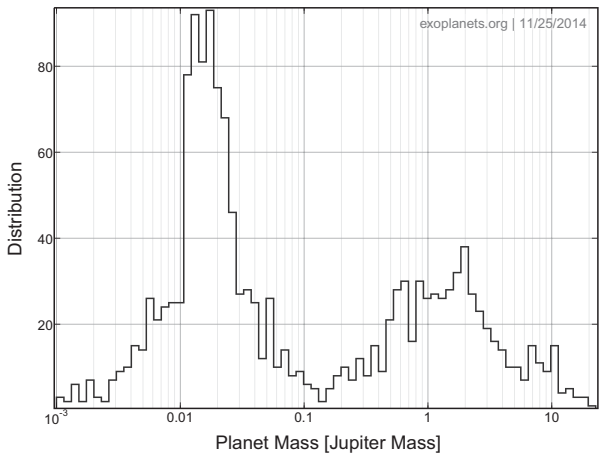

Figure 7. Histogram of confirmed exoplanet masses. The first peak at 0.01–0.03 M_J is mainly contributed by transit detections, and the second peak at 0.5–3 M_J mainly by RV detection. Each detection method does reveal both peaks, though at slightly different positions. For the RV method the peaks are at 0.04–0.05 M_J and 2 M_J, whilst for the transit method they are at 0.01–0.02 M_J and 1 M_J. This plot was generated using the data base of Wright et al. (2011).

exoplanets has two broad but distinct peaks, one at 0.01–0.03 M_J and the other at 0.5–3 M_J. See Fig. 7, which only includes RV and transit discoveries. With, respectively, about 1000 and 500 planets, the dominant population is reversed between transit and RV discovery techniques, probably due to their different mass and orbital radii sensitivities. But nevertheless both show the two peaks, and even more clearly a distinct minimum at 0.1–0.2 M_J. There is possibly a third minor peak at 7–10 M_J, which, despite its questionable significance, is also the mass range in which most exoplanets found via direct imaging lie.

Most interestingly for the purpose of this paper is that there are only a handful of exoplanets with mass $\geq$10 M_J. Despite the good sensitivity of the RV technique to bodies in this mass range, it is possible that it has not fully sampled the parameter space where these bodies might exist beyond a radius of about 5 au, the region of interest for HD100546. However, many imaging surveys of solar-like stars, with ages spanning tens to hundreds of Myr, have been sensitive enough to detect such bodies at separations beyond 5 au, and their rarity has essentially been confirmed (e.g. Lowrance et al. 2005; Kouwenhoven, Brown & Kaper 2007; Lafreniere et al. 2007; Apai et al. 2008; Kraus et al. 2008; Nielsen et al. 2008; Metchev & Hillenbrand 2009; Nielsen & Close 2010; Evans et al. 2012; Biller et al. 2013; Janson et al. 2013; Nielsen et al. 2013; Wahhaj et al. 2013; Chauvin et al. 2015; Ma & Ge 2014). Indeed, most of these studies have found results consistent with the statement of Brandt et al. (2014), namely that with high confidence only a few per cent of stars host planets with mass 5–70 M_J at radii 10–100 au. The paucity of such bodies has been termed the 'brown dwarf desert', the driest part of which was determined to be around 30 $\pm$ 20 M_J by Grether & Lineweaver (2006).

4.9.2 HD100546 planets – limits and putative detections

For HD100546 itself, from *HST* STIS data Grady et al. (2005) concluded they would have easily detected a young chromospherically active low-mass stellar companion, of spectral type earlier than about M5, within 2.5–10 au. It is difficult to put hard constraints on the mass of a companion they could or could not have detected. On the one hand, they used AT Mic as a template, an 8–20 Myr binary whose components are flare stars with spectral types of M4–4.5 Ve and masses of 0.16–0.31 $M_\odot$. On the other hand, their upper bound to HD100546's chromospheric and transition region flux meant they could not have detected an 8–10 Myr 0.06 $M_\odot$ brown dwarf. Thus, the suggestion is that they might have detected a companion with a mass between about 60 and 150 M_J, especially if its age was less than 5–10 Myr.

Outside of the cavity, Quanz et al. (2013a) and Currie et al. (2014) directly imaged a putative giant protoplanet (HD100546 b) at 3.8 μm (L' filter) at an observed separation of 47 $\pm$ 4 au and PA of $\sim$10°. This was deprojected to 53 au by Quanz et al. (2015) using the ALMA-inferred disc inclination and PA from Pineda et al. (2014), or 68 au by Quanz et al. (2013a) using the NIR scattering disc figures from Quanz et al. (2011). The emission consists of a point (or slightly extended) source embedded in a finger-like region extending along a similar PA. Assuming the point source to arise from photospheric emission of a massive planet or substellar object, the authors infer a mass of around 15–20 M_J for an age of 5–10 Myr. Quanz et al. (2015) recovered the putative planet at 3.8 μm as well as at 4.8 μm (M' filter), but despite having the requisite sensitivity they failed to detect it at 2.1 μm (K_S filter), and similarly for Boccaletti et al. (2013) at 2.15 μm.

Interestingly, the 3.8 μm photometry of Quanz et al. (2013a, 2015), despite using the same instrument and filter, resulted in significantly discrepant magnitudes, namely 13.2 $\pm$ 0.4 and 13.92 $\pm$ 0.10, respectively. Our own mass estimates from the photometry, using the AMES COND models (see below) suggest that for L' = 13.2 the mass is 16–21 M_J for an age of 5–10 Myr, consistent with 17–21 M_J implied by the M' = 13.33 measurement but inconsistent with the upper limit of 9–12 M_J for K_S > 15.43. On the other hand L' = 13.92 implies a mass of 11–14 M_J, consistent with the K_S upper limit mass but inconsistent with the M'-implied mass. Such inconsistencies, plus other properties such as its morphology, prompted all authors to favour a model wherein the source is a planet still in the process of formation, and where the point or slightly extended component consists of the planet plus its circumplanetary disc. The luminosity provided by the circumplanetary disc means that the planet mass could be much less than 10 M_J and perhaps as low as 1 M_J (Currie et al. 2014).

In addition to the finger-like extension surrounding HD100546 b, all authors also found another emission feature at a similar separation from the star and with a similarly extended morphology – though without an obvious point source component – $\sim$90° away on the southeast side of the disc. It is almost certainly due to thermal emission, rather than scattering, as none of Boccaletti et al. (2013), Avenhaus et al. (2014b) or Quanz et al. (2015) detect it at K_S, and it appears to brighten from L' to M'. Currie et al. (2014) suggest it may be an additional spiral arm of the HD100546 disc, though it would differ from the other known spiral arms which are only seen in scattered radiation (and thus are disc 'surface' features, e.g. Grady et al. 2001 and Ardila et al 2007).

At $\sim$50 au from the central star the emission cannot be reprocessed stellar radiation and so its heating mechanism is currently unknown. By extrapolation we also suggest that the origin of the extended emission surrounding HD100546 b is also unknown, though Quanz et al. (2015) suggest it arises from localized compressional heating of the HD100546 circumstellar disc. Perhaps even more controversially, but given the unknown physics behind the extended emission, we suggest that the nature of the feature identified as the protoplanet HD100546 b remains open to interpretation. Having said that, the fact that it is comoving with HD100546 means it is

certainly physically associated with it, e.g. a feature within the circumstellar disc. Notably, no sign of either feature is seen in our mm-wave data (see Section 4.11).

Finally, the work of Ardila et al. (2007) using *HST* and Boccaletti et al. (2013) provides stringent constraints on the presence of other planetary-mass bodies from 90 to 1200 au and 50 to 400 au, respectively. Essentially they were able to exclude the presence of 5–10 Myr old objects with mass $\geq$20–30 M_J at around 50 au, with progressively lower limits with increasing separation, down to only $\sim$2 M_J at 150 to 400 au and 4 M_J beyond 400 au.

4.9.3 Single companion to HD100546 interior to 13 au?

As previously noted, the mere existence of a gap – or cavity in the case of HD100546 – may suggest the presence of a massive orbiting body, whilst the gap width (cavity radius) may be used to infer the body's mass. For instance, Mulders et al. (2013b) performed hydrodynamic modelling, and found that a 20–80 M_J body, with a preferred value of 60 M_J and orbiting at 8–10 au, well reproduced the surface density profile of the rounded wall. This puts the gap-sculpting body firmly in the brown dwarf category.

A similar mass can be found without recourse to hydrodynamic simulations. Dodson-Robinson & Salyk (2011) found that, within 0.5 Myr, the maximum gap opened by a planet would not exceed about five Hill radii, where the Hill radius is expressed as $R_H = r_p \times (M_p/3M_*)^{1/3}$, with r_p and M_p being the planet's orbital radius and mass, respectively, and M_* the stellar mass. For a 50 M_J body orbiting at 13 au from a 2.4 $M_\odot$ star R_H is $\sim$2.4 au, so that a gap is opened from 1 to 25 au, consistent with the 1–7 mm data for HD100546.

There is however a potential problem with such a massive single body being present in the HD100546 disc cavity. It is very close to the lower limit found by Grady et al. (2005) discussed above, and may even exceed it assuming a younger age than 8–10 Myr. For instance, according to the Baraffe et al. (2003) evolutionary models, at 1 Myr a $\sim$25 M_J body has about the same luminosity of $\sim10^{-4}$ $L_\odot$ as a 50 M_J body at 5 Myr or 70 M_J at 10 Myr. There is in fact good evidence that HD100546 could be much younger than 10 Myr, essentially based on the presence of an outflow and a relatively high-mass accretion rate (see below and Appendix C, available online as supplementary material).

For HD100546, the 'single companion' situation can be dramatically improved by using the work of Pinilla, Benisty & Birnstiel (2012). They found that by including grain evolution in their hydrodynamical simulations the location of the pressure bump, i.e. where the large dust grains pile up, can instead be at about 10 Hill radii for a body with mass $\geq$5 M_J. In this case, a 10 M_J planet orbiting at 13 au has an R_H of 1.4 au, and thus can open the gap out to 25 au seen in HD100546.

Yet this also poses a problem given that such bodies are exceedingly rare, as discussed above. Also, it is still only a single body. The example of our own Solar system tells us there are four gas giants orbiting within about 30 au, and around two-thirds of the $\sim$1500 currently known and confirmed exoplanets are part of a multiplanet system (Wright et al. 2011). So why would HD100546 only host a single planet within its disc cavity? Whilst there is still disagreement in the literature about how large a cavity a single body can open, there is overall agreement that multiple (Jupiter mass) bodies will each open their own gap, which could overlap to produce a much broader cavity (e.g. Zhu et al. 2011).

In this context, the case of the LkCa 15 planet is instructive. It is so far the only directly imaged exoplanet candidate within a transitional disc cavity, whose cavity radius is $\sim$50 au (Andrews et al. 2011a,b; Kraus & Ireland 2012). The suspected planet orbital radius and mass are $\sim$16 au and 6 M_J, respectively, and from its spatially resolved morphology is thought to be still in the process of formation. Second epoch observations presented in Ireland & Kraus (2013) show rotation by an amount consistent with that expected, whilst new *M*-band data allowed a refined mass estimate to be made of 1–3 M_J. Using a stellar mass of 1.2 $M_\odot$, and even taking the higher mass estimate of 6 M_J at an orbital radius of 16 au, gives a Hill radius of $\sim$1.9 au, insufficient to clear the entire cavity even using the 10R_H constraint. The situation is made even worse if a lower mass for LkCa 15b is assumed. Furthermore, given its presumed youth, i.e. less than 1 Myr, there has probably been sufficient time to clear a gap but not necessarily to clear an entire cavity all the way to the central star (e.g. Dodson-Robinson & Salyk 2011).

4.9.4 Multiple companions to HD100546 within 13 au?

Along with the arguments presented above, the hypothesis that HD100546 may host a multiplanet system within its disc cavity is driven primarily by the requirement to pass a potentially significant amount of material from the outer to inner disc and then on to the star, whilst still maintaining the 'appearance' of an empty cavity from $\sim$1–13 au. There are various estimates in the literature for the mass accretion rate of HD100546, but it is the lower figure of less than a few times 10^{-9} $M_\odot$ yr^{-1}, and possibly an order of magnitude lower, from Grady et al. (2005), that appears to have gained most acceptance. But how reliable is it?

First, this estimate was only indirect, based principally on a comparison of the HD100546 *HST* STIS ultraviolet spectrum to that of two other Herbig Ae/Be stars with 'known' accretion rates (HD163296 and HD104237). On the other hand, modelling of IUE spectra produced estimates as high as $\sim5 \times 10^{-7}$ $M_\odot$ yr^{-1} (Talavera, Blondel & Tjin A Djie 1994; Blondel & Djie 2006). Most recently, an accretion rate of log $M_{acc} = -7.23 \pm 0.13$, or $\sim(6 \pm 2) \times 10^{-8}$ $M_\odot$ yr^{-1}, was determined by Pogodin et al. (2012). Finally, our own 3 and 6 cm radio observations, coupled with an analysis of ISO hydrogen recombination line data, suggests a mass outflow rate of a few $\times 10^{-8}$ $M_\odot$ yr^{-1}, and thus an accretion rate around 10 times higher (applying the canonical conversion factor; e.g. Calvet 2004). Appendix C – only available online as supplementary material – contains further details on the HD100546 accretion rate.

We thus conclude that the mass accretion rate of HD100546 is at least 5×10^{-8} $M_\odot$ yr^{-1}, which then puts it in better agreement with correlations of accretion rate with stellar mass for Herbig Ae/Be stars, e.g. in Donehew & Brittain (2011) and Garcia Lopez et al. (2006). But this presents a significant problem when trying to unite it with other properties of HD100546. Most specifically, the total mass of gas and dust of the compact inner disc is at most about 10^{-8} $M_\odot$, with estimates including a few $\times 10^{-10}$ $M_\odot$ of small dust grains from $\sim$0.25 to 4 au (Benisty et al. 2010; Tatulli et al. 2011), 5.1×10^{-9} $M_\odot$ of small dust grains from 0.3–9.8 au, (Bouwman et al. 2003), and $\leq1.5 \times 10^{-8}$ $M_\odot$ of gas within the entire cavity (Brittain et al. 2009).

The obvious implication is thus that the compact inner disc, and even the cavity up to 13 au, would be completely drained of material in much less than a year, or at best on the time-scale of about a year. So they must evidently be continually replenished from the

outer disc. But how? Dodson-Robinson & Salyk (2011) find that the interconnecting tidal streams from multiple planets provide a way for an abritrary amount of mass transfer to occur, through an apparently optically thin hole, than would otherwise be the case for a single planet. For instance, they present a model in which at least a factor of 2 times more small dust particles can exist within a cavity if it is 'hidden' in geometrically thin but optically thick streams (i.e. with a low filling factor for its thermal emission). Inclusive of solid mass potentially being cloaked in much larger particles, such as pebbles, rocks, boulders and planetesimals, there could be much more material in the cavity than could be seen with current observational techniques.

This scenario has significant attraction for HD100546, but not merely to account for the relatively high-mass accretion rate and apparently (almost) empty cavity. It may also bear on the conjecture by Grady et al. (1997) and Vieira et al. (1999) that much of the accreting gas is associated with star-grazing bodies, possibly comets or asteroids (although this model has been questioned, but not excluded, by Beust, Karmann & Lagrange 2001; Deleuil et al. 2004). In this context, Dodson-Robinson & Salyk (2011) note that their multiplanet model for transition discs predicts that the observed small dust (e.g. in the mid-IR) is non-primordial, and instead the product of collisional grinding of planetesimals. This is a very real possibility for HD100546 given the almost identical nature of its mid-IR spectrum to that of Comet Hale–Bopp in our Solar system (Malfait et al. 1998b).

Also, that such a large amount of material must be crossing the cavity to refuel the inner disc and subsequently accrete on to the star, possibly episodically (or at least not in a continuous manner), may account for the numerous examples of variability seen for this system. Such variability is observed over different time-scales of minutes, hours, days, months and years. Examples include accreting and outflowing gas profiles (Pogodin 1995; Grady et al. 1997; Vieira et al. 1999; Deleuil et al. 2004; Guimaraes et al. 2006), optical polarization (Yudin & Evans 1998; Clarke, Smith & Yudin 1999) and radio emission (Appendix D, only available online as supplementary material). In particular, Vieira et al. (1999) detected an Algol-like *uvby* photometric minima coincident with a H α line profile variation. Such Algol-like minima for Herbig stars are commonly interpreted as extinction variations, related to discrete events of localized material passing in front of the star.

4.10 HD100546 in the context of other transition disc systems

Consistent with the dearth of massive exoplanet or brown dwarf companions at large orbital radii towards main-sequence stars, and despite the requisite sensitivity being achievable, it is proving difficult to find 10–30 $M_{\rm J}$ companions orbiting transition disc host stars, especially within but also exterior to the cavity. For instance, although statistically limited Andrews et al. (2011a) noted that for at least half the then known (12 or so) transition discs – for which a search had been conducted – there were no companions found with mass $\geq$20–30 $M_{\rm J}$ interior to the cavity, and thus that could be solely responsible for its sculpting. See also Kraus & Ireland (2010) where the limits are expressed as 5–8 $M_{\rm J}$ at 5–30 au.

4.10.1 Known planet or low-mass brown dwarf companions

As previously noted, only LkCa 15 has a directly imaged protoplanet candidate within the disc cavity. Otherwise, the $\sim$140 au radius cavity of HD142527 hosts a stellar mass companion with a mass of 0.1–0.4 $M_{\odot}$ at a radius of about 13 au (Biller et al. 2012; Close et al. 2014; Rodigas et al. 2014). But Casassus et al. (2012) found no planetary mass companions $\geq$12 $M_{\rm J}$ at radii of 14–35 au, whilst Rameau et al. (2012) excluded brown dwarfs or the most massive giant planets at radii $\geq$40–50 au, and planets $\geq$6–10 $M_{\rm J}$ or $\geq$3–5 $M_{\rm J}$ at radii beyond $\sim$100 au or 200 au, respectively. Also, a companion brown dwarf candidate was inferred in the cavity of the T Cha disc by Huelamo et al. (2011), but was not confirmed despite multiple attempts (e.g. Olofsson et al. 2013; Sallum et al. 2015) and has recently been shown by Cheetham et al. (2015) to be a scattering feature of the disc itself.

A massive brown dwarf and a massive planet/low-mass brown dwarf have also been claimed within the disc of HD169142 by Reggiani et al. (2014) and Biller et al. (2014). This disc includes a cavity extending to 20–25 au, then a 15–20 au thick ring of material followed by an annular gap from 40–70 au (e.g. Quanz et al. 2013b; Osorio et al. 2014). However, both postulated bodies have potentially serious problems. The locations of the independent L' detections of the massive BD only agree at the limits of the respective uncertainties, 0.156 ± 0.032 arcsec at PA $= 7\overset{\circ}{.}4 \pm 11\overset{\circ}{.}3$ of Reggiani et al. and 0.11 ± 0.03 arcsec at PA $= 0^{\circ} \pm 14^{\circ}$ of Biller et al. The Reggiani et al. location puts the body at 22.6 ± 4.7 au, either just inside or even within the 15–20 au wide dusty ring. Furthermore, neither author detected anything at z', J, H and K_S, despite the requisite sensitivity being easily achieved. Thus, much like the case of HD100546 b discussed previously the L' detection cannot be due to photospheric emission from a substellar or planetary mass companion, and instead is more likely to either be a planet in formation (Reggiani et al.) or a feature of the disc itself heated by an unknown mechanism (Biller et al.). Similarly, a second possible body detected by Biller et al. at H and K_S at a separation of $\sim$0.18 arcsec (26 au) and PA $\sim 33^{\circ}$ is also located within the ring of material and lacks a concomitant detection at z'.

4.10.2 Summarizing stellar and disc properties of transition systems

Since no such compendium exists to our knowledge, in Table 3 we have summarized the properties of most known transition disc systems with a mm-resolved cavity, plus the observational limits on the mass and location of companions. In addition to objects already 'catalogued' as transition discs, we have included several other sources based on possible nulls in their deprojected visibilities. These include DS Tau (Pietu et al. 2014) as well as BP Tau, CI Tau and FT Tau (Guilloteau et al. 2011).

The first five columns of Table 3 are the object name, assumed distance, and the ranges found in the recent literature for the stellar age, mass and accretion rate. In some cases, the spread in these values is large, even up to a factor of 2 in the mass and a decade or so in the age and accretion rate. The mass and age can be critically dependent on the particular stellar evolutionary model used, whilst the accretion rate may be dependent on the tracer used as well as in some cases being time variable. Sources for these stellar parameters are provided in Appendix E, and similarly for the disc parameters in columns 6–10, described below.

The sixth column of Table 3 provides the deprojected $u - v$ distance at which the first null in the real part of the visibility occurs, as well as the inferred radii using equations A9 and A11 in Hughes et al. (2007). Whilst the null position is explicitly stated by some authors, in other cases it has been read directly off their visibility plots. Different authors may also have observed the same

Table 3. Companion limits to transitional disc host stars.

Star	d (pc)	Age (Myr)	Mass ($M_\odot$)	$\dot{M}$ ($\times 10^{-8}$ $M_\odot$ yr^{-1})	Null,R_{11},R_9 (kλ, au, au)	Gap R (mm) (au)	Gap R (SED) (au)	Gap R (N/MIR) (au)	Gap R (gas) (au)	Mass req'd (M_J)	Mass limit (M_J)	Sep. (au)	Refs.
HD100546	97	3.5–10	2.4	6–50	320 [25,18]	[25]	10	12–14	13	60,7.5	60–150	2.5–10	1
					290 [27,20]	**26**					100–160	30	2
											9–12	48	3
											6–9	70	2
											4–6	90	2
											2–4	≥110	2,4
LkCa 15	140	2–5	1.1	0.14–0.40	145 [76,56]	**50**,46	*39*	50	13–23	28,3.5	16–20	14	5
						[61]	46,58				13–17	16.1	5
											10–14	18.2	5
											6–12	28–37.8	5,6
											4–9	42–56	5,6
											4–6	56–77	5,6
											2.5–5.5	≥80	5,6
											20–30	2.8–5.6	7
											10–20	5.6–22.4	7
											19–30	22.4–44.8	7
HD142527	145	1–10	2.2	6.9–20	78 [148,108]	[140]	130	143	90	50,6.3	27–66	29–44	8
											20	77	9
											6.5	101	9
											9	130	9
											5	200	9
											2.5	218	9
HD169142	145	3–12	1.7	0.31–4.0	NG	[25–30]	23	20–25			28–52	26.1	10
						40–70					7–12	26.1	10
											14–20	49.3	11
											13–18	87	12
											6–11	145	12
HD135344	142	8 ± 6	1.7	0.54–2.0	170 [66,48]	**46**,39	30,45	28	0.5	43,5.3	230	14	13
						[60–65]					85	36	13
											50	43	13
											21	57	14
											16	71	14
											12	85	14
											9	114	14
											7	142	14
MWC 758	200	3–5	2.0	6–89	190 [83,61]	**73**	≤1	≤20	≤30	50,6.3	≤80	0–60	15
						[100]					80	30	15
											45	40	15
											15	50	15
											8	100	15
											3	200	15
											2	≥300	15
GM Aur	140	1–7	1.4	0.50–1.0	225 [49,36]	**28** [29]	20–24	20.5	19 ± 4	25,3.1	19–35	2.8–5.6	7
											9–22	5.6–22.4	7
											22–40	22.4–44.8	7
J160421.7 −213028	145	3.7–11	1.0	≤0.001	125 [90,66]	72,**79**		63	31	25,3.1	22–29	2.9–5.8	16
						[80]					15–19	5.8–23.2	16
											19–28	23.2–46.4	16
											5–73	300–60	17
DM Tau	140	3–8	0.55	0.20–1.1	385 [29,21]	**19** [16]	3	≤15.5		14,1.7	18–33	2.8–5.6	7
											8–18	5.6–44.8	7
UX Tau A	140	1	1.5	0.10–4.7	330 [33,25]	**25** [22]	*30*	≤23		38,4.7	31	2.8–5.6	7
							56,71				17	5.6–22.4	7
											35	22.4–44.8	7
RY Tau	140	0.5–8	2.0	2.2–25	625 [18,13]	[**14**]	18			50,6.3	105	0.35–4.2	18
											40–77	2.8–44.8	7
LkHa 330	250	3	2.4	0.16–1.6	215 [92,67]	**68**,47,41	50		4	60,7.5	50	10	19
						[77,100]					25	Cavity	20
SR21 A	125	1–5	2.0	≤0.14–1.3	210 [47,34]	37,**36**,33	18	≤12	7	50,6.3	40–60	≥18	21
						[35]					50	≥5	19
											21	Cavity	20
WSB 60	125	0.9–3	0.2	0.10–0.37	370 [27,20]	**15** [15]				6.3,0.8	95–160	2.5	22
					350 [28,21]	20					21–27	18.75	23
					350 [28,21]	20					15–21	62.5	23

Table 3 – *continued*

Star	d (pc)	Age (Myr)	Mass ($M_\odot$)	$\dot{M}$ ($\times 10^{-8}$ $M_\odot$ yr^{-1})	Null,R_{11},R_9 (kλ, au, au)	Gap R (mm) (au)	Gap R (SED) (au)	Gap R (N/MIR) (au)	Gap R (gas) (au)	Mass req'd (M_J)	Mass limit (M_J)	Sep. (au)	Refs.
Oph IRS48	121	1	2.0	0.32	NG	**63**		30–60	20–30	55,6.9	150	2.5	22
											100	18.75	23
											50	62.5	23
SR24 S	125	0.2–2.4	2.0	3.0–7.4	230 [43,31]	**29**				35,4.4	75	2.5	22
					200 [49,36]	32					100	12.5–100	24
DoAr 44	125	1–7	1.0	0.63–0.93	230 [43,31]	**30** [28]	36			30,3.8	70–90	2.5	22
					215 [46,34]	33					80–120	12.5–62.5	23,24
J1633.9	120	2	0.7	0.013	280 [34,25]	**23 ± 2**	8 ± 2			18,2.2	10	2.4–4.8	25
−2442						[23]					6	>4.8	25
PDS70	140	5–10	0.8		NG	[80]		65		20,2.5	3–6	18.2	26
											2–4	28	26,27
											1.8–3.5	56	26,27
											1.3–3.0	84	26,27
											1.2–2.6	>140	26,27
Sz91	200	5	0.5	0.008	135 [117,86]	**97**		65 ± 4	≤28	13,1.6	80–100	30	30,31
						[86 ± 25]							
J1615-3255	185		1.2	0.04–0.32	280 [52,38]	**30** [27]	2–4			28,3.5			
CQ Tau	100	5–10	1.5	≤0.50–11.2	280 [28,21]	21				38,4.7			
DS Tau	140	4–7	0.7	0.16–4.1	300 [37,27]	15 ± 5			30 ± 9	18,2.2	40–80	2.8–5.6	7
						20 ± 4					20–36	5.6–11.2	7
											24–43	11.2–22.4	7
											30–60	22.4–44.8	7
BP Tau	140	0.9–3.2	0.8	1.3–81	450 [25,18]	18				20,2.5	40–45	2.8–5.6	7
											21–31	5.6–22.4	7
											44–51	22.4–44.8	7
CI Tau	140	2	0.8	1.5–6.5	330 [33,25]	25				20,2.5	64–78	2.8–5.6	7
											26–35	5.6–22.4	7
											32–38	22.4–44.8	7
FT Tau	140	1.6	0.30	3.1	500 [22,16]	16				7.5,0.9	29–34	2.8–5.6	7
											12–20	5.6–44.8	7
T Cha	100	3–10	1.5	0.4	NG	20	7.5,15	12 ± 2		38,4.7	28–55	1–10	28,29

References for the stellar and disc parameters are provided in Appendix E. Numbered references for the planet detection limits are the following: (1) Grady et al. (2005) (2) Boccaletti et al. (2013) (3) Quanz et al. (2015) (4) Ardila et al. (2007) (5) Thalmann et al. (2010) (6) Bonavita et al. (2010) (7) Kraus et al. (2011) (8) Casassus et al. (2012) (9) Rameau et al. (2012) (10) Biller et al. (2014) (11) Reggiani et al. (2014) (12) Grady et al. (2007) (13) Vicente et al. (2011) (14) Grady et al. (2009) (15) Grady et al. (2013) (16) Kraus et al. (2008) (17) Ireland et al. (2011) (18) Pott et al. (2010) (19) Brown et al. (2009) (20) Andrews et al. (2011a) (21) Follette et al. (2013) (22) Simon et al. (1995) (23) Ratzka, Kohler & Leinert (2005) (24) Ghez, Neugebauer & Matthews (1993) (25) Cieza et al. (2012) (26) Hashimoto et al. (2012) (27) Riaud et al. (2006) (28) Olofsson et al. (2013) (29) Huelamo et al. (2011) (30) Romero et al. (2012) (31) Canovas et al. (2015).
Note: NG means Not Given.

target and found a slightly different null position, the reason for which may simply be due to different choices for the disc PA and inclination used in the deprojection. This is apart from the case of HD100546 itself, for which the null position almost certainly changes between the ALMA 340 GHz observation of Walsh et al. (2014) and our ATCA observations at 44 GHz.

Equation A9 in Hughes et al. is valid for a disc whose outer radius is significantly larger than the inner (i.e. cavity) radius, and where the addition of the power-law indices for surface density $\Sigma \propto R^{-p}$ and temperature $T \propto R^{-q}$ is in the range $1 \leq p + q \leq 3$. A value of 3 has been assumed for all sources. This holds no particular physical significance, and indeed such a simple power law for the surface density is generally no longer considered appropriate for protoplanetary discs. See for example Andrews et al. (2009) for further details. Equation A11 of Hughes et al. is instead strictly valid for a thin ring of constant brightness, where $\Delta R/R \ll 1$.

Columns 7–9 give the various estimates for the cavity radius, derived from millimetre imaging, modelling of the infrared SED, and directly from near- and/or mid-infrared images, all from dust continuum. The mm-measured cavity radius is differentiated between that inferred from (i) modelling within the respective literature of the interferometer visibilities in conjunction with the entire IR–mm SED, and (ii) the peak-to-peak separation along the disc major axis, either stated by authors or derived from their images and given here in square brackets. Our preferred value is given in boldface. For some objects, there are two or more estimates of the SED-inferred cavity size, which in cases like LkCa 15 and UX Tau A is due to different assumptions by respective authors for the central star properties such as spectral type (Espaillat et al. 2010). The most recent – and thus preferred – SED values for these two stars are given in italics, from Espaillat et al. (2011), and thus resolves the otherwise discrepant (and probably unphysical) directly observed and model values. Column 10 instead gives the hole radius inferred using gas tracers, from either infrared ro-vibrational or millimetre rotational spectroscopy.

Clearly neither equation A9 nor A11 of Hughes et al. (2007) is generally appropriate for deriving the 'true' cavity size. From a purely empirical perspective, when $p + q = 3$ equation A9 does appear to provide an estimate in better agreement with the 'true' cavity size determined from the detailed modelling. However, in a few cases (e.g. HD100546 and HD142527) the assumption of a thin ring seems to hold true. This is perhaps not so surprising for HD142527 given its large cavity radius. Also, whilst it obviously indicates the presence of a cavity or gap, infrared SED modelling is not generally a reliable estimator of its size, at least compared to that measured at millimetre wavelengths. This may in some cases be due

to inappropriate stellar parameters in the SED model, but in other cases is probably related to the fact that the IR SED is primarily sensitive to the small grain population whilst the millimetre regime is sensitive to larger grains. And as we have seen for HD100546, but also for HD135344, SR 21A, GM Aur and perhaps also DM Tau, the near- and/or mid-IR images indeed show a cavity size more consistent with the SED value.

4.10.3 Observational limits of companion masses in transition disc systems

Column 11 of Table 3 provides estimates of the mass of a single orbiting body capable of clearing the observed mm cavity. The two estimates are based on the assumption that the body could clear a gap out to 5 and 10 Hill radii, as postulated by Dodson-Robinson & Salyk (2011) and Pinilla et al. (2012), respectively. The orbital radius of the body is placed in the middle of the cavity. For comparison, columns 12 and 13 of Table 3 provide observed limiting masses and separations of possible orbiting bodies within the disc, whilst column 14 provides references for the data to derive these companion limits.

The limiting masses and separation were typically derived from either near-IR SAM or coronagraphic imaging coupled with adaptive optics and angular differential imaging. Where such typically very recent data was not available we also considered lunar occultation or speckle imaging observations, which were much less sensitive to giant planets or low-mass brown dwarves, but were at least useful in ruling out high-mass brown dwarf or low-mass stellar companions. Respective authors provided companion detection limits – typically quoted to 3σ–5σ – as a function of radius in arcseconds from the central object, either in terms of a flux ratio or magnitude difference. These were converted to absolute magnitudes which were then compared to evolutionary models of the photospheric emission from massive exoplanets and/or brown dwarfs (see below).

For consistency, where possible we have used the respective author's data to derive our own planet mass estimates, even though those authors may also have provided such estimates. This was not possible for LkHα 330 or SR21 A, for which Brown et al. (2009) and Andrews et al. (2011a) quoted private communications for an upper limit of the secondary mass. We generally find good agreement between our own and literature values, with any discrepancies likely resulting from using different ages and/or central stellar mass (where the planet mass limit is expressed as a secondary-to-primary mass ratio). In only one case, RY Tau, do we find a significant difference. Kraus et al. (2011) quote a mass ratio of 0.009 within most of the cavity, which translates into a secondary mass of 14 $M_{\rm J}$ using their preferred primary mass of 1.46 $M_{\odot}$, or up to 19 $M_{\rm J}$ assuming a stellar mass of 2 $M_{\odot}$ also found in the literature. However, using their observed H-band magnitude difference and an age even as young as 1 Myr, we instead find an upper limit on the secondary mass of $\sim$40 $M_{\rm J}$.

We tested the model isoschrones found at http://phoenix.ens-lyon.fr/Grids/, including the DUSTY and COND variants described in Baraffe et al. (2003), Allard et al. (2001) and Chabrier et al. (2000), as well as the BT-SETTL grid described in Allard, Homeier & Freytag (2012). We direct the reader to these papers for a full explanation of the photospheric physics and chemistry treated in the models. Briefly however the DUSTY and COND variants represent extreme cases wherein the formation of dust in the equation of state is included in both, but only in DUSTY is dust scattering and absorption in the radiative transfer equation taken into account, and where it is further assumed that the dust remains in the photosphere (i.e. there is negligible settling). On the other hand, the COND variant assumes all the dust has disappeared from the photosphere via gravitational settling, and thus neglects dust opacity in the radiative transfer. The BT-SETTL variant includes such settling. In practice, and consistent with Boccaletti et al. (2013) in their study of HD100546, we found little difference between these model variants.

These grids are of particular utility as they provide predicted absolute magnitudes in different filters for a wide variety of optical and infrared instruments at many different observatories around the world. Further, the grid spacing for age is only 1 Myr in the age range of 1–10 Myr relevant for most of our sample, whilst the grid spacing for the secondary mass varies between 0.001–0.01 $M_{\odot}$ in the mass range relevant to giant planets and brown dwarves. Of course, these grids are for only one of the two main postulated modes of planet formation, namely gravitational instability within the disc rather than core-accretion, otherwise generally classified as hot- and cold-start models, respectively. The formation mechanism of giant planets in the radius range of interest here is still a hotly debated topic, e.g. Spiegel & Burrows (2012), Janson et al. (2011) and Dodson-Robinson et al. (2009). But what is certain is that core-accretion/cold-start giant planets are predicted to be much fainter – by several magnitudes in the near-IR – than their gravitational-instability/hot-start counterparts, and thus to not be generally detectable with current techniques (e.g. Vigan et al. 2012).

Another assumption in our treatment is that there is no differential extinction between the primary and secondary bodies. This is probably unrealistic, but necessitated by the simple fact that assigning any such number would be a guess. If however the putative planet suffers more (less) extinction than the star then the mass we derive would be lower (higher). Further, we have assumed that any planet would be the same age as the star itself. Whilst this seems like a reasonable assumption we note that the directly imaged planet candidates so far discovered towards transition disc sources, be they internal (LkCa 15) or external (HD100546) to the cavity, or somewhere in between (HD169142), have all been assessed to be much younger than the star itself.

With the aforementioned caveats in mind, and by way of example, in the case of MWC 758 any body within 60 au of the star must have a mass less than the most massive brown dwarfs (Grady et al. 2013), otherwise it would have been detected. Also, at separations of 50, 100, 200 and 300 au any body must be less massive than 15, 8, 3 and 2 $M_{\rm J}$, respectively (or alternatively a body more massive than 15 $M_{\rm J}$ would have been detected at any separation greater than 50 au and similarly for the other mass/separation combinations). In several cases (e.g. HD100546, LkCa 15, HD142527) several data sets were available, which used either a different imaging technique and/or a different filter, but which gratifyingly gave consistent secondary mass limits.

Putting all the data together, Table 3 shows that in all cases where sufficient sensitivity has been attained (11 of 27) the mm-derived cavity could not have been carved by a single body if its clearance radius was only five Hill radii. Thus, under the $5R_{\rm H}$ scenario these cases would likely require multiple giant planets to carve the disc gap. Further, in one of these cases, namely PDS 70, even a body which could clear out to $10R_{\rm H}$ is excluded at the younger end of the age range for its parent cloud Centaurus.

However, perhaps the most striking feature of the compilation in Table 3 is that massive gas giant planets and/or low-mass brown dwarves are rare at large orbital separation from their host star.

For instance, for 22 sources there was sufficient sensitivity to have detected a body of 50 M_J or less somewhere in the orbital range of greater than about 3 to 60 au (dependent on the specific sensitivity of individual targets). But as previously noted, for only 3 of those 22 sources (i.e. LkCa 15, HD100546 and HD169142, or ∼14 per cent) has a planet detection been made. Without pursuing a rigorous statistical treatment this is remarkably similar to the direct imaging detection rates cited in 4.9.1 for typically much older systems. Interestingly it also agrees with the work of Cieza et al. (2012), who suggest that only ≤18 per cent in their sample of 74 Spitzer-selected transition discs in nearby clouds are best explained by the dynamical interaction of recently formed giant planets.

Indeed, the likely direct descendents of transition discs are the gas-poor debris discs, whose dust population – without ongoing planetesimal collisional replenishment – would otherwise be depleted on relatively short time-scales by inward spiral and radiative blow-out. Wahhaj et al. (2013) conducted a direct imaging survey for giant planet companions of 57 debris discs, finding none and concluding that at 95 per cent confidence <13 per cent have a ≥5 M_J planet beyond 80 au, and <21 per cent have a ≥3 M_J planet outside of 40 au, using hot-start evolutionary models.

Overall, we believe these results are best explained by a scenario wherein the centrally cleared gaps and/or broad cavities in most – not necessarily all – transition disc and (by extension) debris disc systems are created by overlapping gaps cleared by multiple one-to-several-Jupiter-mass bodies rather than a single many-Jupiter-mass body. From a statistical standpoint then, it is unlikely that only a single body is responsible for carving out the ∼25 au radius mm-wave cavity within the HD100546 disc.

4.11 Why no direct planet detection or second ring of emission at 7 mm?

There is no evidence in Figs 1 or 3 for emission directly associated with an orbiting body, such as HD100546 b at ∼47 au (Quanz et al. 2013a, 2015; Currie et al. 2014). HD100546 b has been conjectured by Quanz et al. (2013a, 2015) and Currie et al. (2014) to be a protoplanet, one still in the process of formation, and thus potentially still embedded in a dust and gas envelope.

Further, apart from evidence for a fainter component of extended emission beyond the ∼50 au radius compact circumstellar disc – as indicated by the difference between compact and extended array fluxes in Table 1 – we do not resolve this into a second ring of emission. The gap between this second ring and the ∼50 au radius disc could have been cleared by the 53–68 au planet (disc inclination dependent), as postulated by Walsh et al. (2014). Our 7 mm extended component could well be in the form of a second ring, but the data is insufficient to go beyond this simple statement.

It is thus interesting to ask why neither the 53–68 au planet (or rather its circumplanetary disc) nor a second ring were detected in our data set.

4.11.1 Upper limit on circumplanetary disc mass

The best 7 mm 3σ sensitivity we achieved is 0.075 mJy beam^{-1} in Fig. 1(e). For silicate dust properties similar to those used in Section 4.6 to calculate the disc mass – i.e. a dust opacity at 7 mm from Draine (2006) with maximum sizes of 0.1, 1, 10 and 100 cm – and a temperature of 40 K, our limiting sensitivity gives ∼2, 1, 2 and 6 Earth masses of dust (or 0.0065, 0.003, 0.0065 and 0.02 M_J; note that fig. 3 of Draine 2006 shows the dust opacity at a wavelength of 7 mm is the same when the maximum size is 1 mm or 10 cm). For a population of silicate grains with a smaller maximum size, i.e. 100 μm or less, the limiting value is ∼16 Earth masses (or 0.05 M_J).

A temperature of 40 K is chosen since Isella et al. (2014) shows that it is the 'asymptotic' temperature at radii ≥1 au in a circumplanetary disc around a 10 M_J planet – regardless of whether it formed by gravitational instability or core accretion – and with a mass accretion rate of ≤10^{-4} M_J yr^{-1}. They found that for accretion rates ≥10^{-6} M_J yr^{-1}, required to build a planet within the disc dispersal time-scale, the circumplanetary disc temperature is set by viscous heating, and is essentially independent of the planet luminosity or irradiation from the central star. Thus, as we might have expected anyway given its large orbital radius, the temperature of the putative circumplanetary disc around the 50–70 au protoplanet is independent of HD100546 itself.

Using the Very Large Array at 7 mm Isella et al. (2014) searched for circumplanetary disc emission from the candidate planet LkCa 15b within the cavity in the disc around LkCa 15, found by Kraus & Ireland (2012). With a 3σ sensitivity about seven times better than ours they were able to set an upper limit of ∼0.1 M_J for the circumplanetary disc mass, inclusive of dust and gas with a mass ratio of 1:100, or simply 0.001 M_J of dust. Taking into account the different sensitivities, this is gratifyingly close to our maximum mass of ∼0.0065 M_J for a disc with grains up to 1 mm in size, despite the use of dust opacities from different published works (inclusive of particular dust components and their relative abundances, as well as the minimum and maximum sizes).

Thus, our work is in very good agreement with that of Isella et al., namely that if there is a circumplanetary disc around forming gas giant planets in or outside the cavity of transition discs then their mass seems to be only a small fraction of the planet mass. In the case of the 50–70 au planet of HD100546, assuming a mass of ≥5 M_J (Quanz et al. 2013a) then the fraction (dust only) is ≤1 per cent, and possibly as low as only several hundredths of a per cent. If the gas-to-dust mass ratio of the circumplanetary disc is as evolved as we argue for the HD100546 circumstellar disc in Section 4.6, i.e. nearer 1 than 100, then these values only increase by at most a factor of several.

4.11.2 A second ring of emission

The outer ring of emission postulated by Walsh et al. (2014) has a maximum surface brightness of around 3 mJy beam^{-1} at 302–346 GHz, judging from the residuals of an inner-ring-only fit in their fig. 4. Assuming a spectral slope similar to the value we find for the inner disc, i.e. $\alpha = 2.45$, the inferred 44 GHz surface brightness is 0.023 mJy beam^{-1}, i.e. about the same as our best rms in Fig. 1(e). Even a slope as flat as $\alpha = 2.0$ only extrapolates to a 7 mm surface brightness of ∼0.055 mJy beam^{-1}. This is below our best 3σ sensitivity of 0.075 mJy beam^{-1} and thus we could not have detected the outer ring in our high-resolution images.

However, if this second ring of 0.023 mJy beam^{-1} filled the beam of our H214 observation of 2009 May 31, which was about 50 times larger in area than the ALMA beam, then its total flux would be around 1.2 mJy. Within the uncertainties this is comparable to the flux difference between the H214 data set, in which HD100546 was a point source, and the 6 km configuration data of 2012 June 20 which resolved the compact disc but would probably have resolved out anything more extended.

5 CONCLUSIONS

From a variety of observations over the last decade or so, spanning wavelengths from the ultraviolet to the infrared and spatial resolutions from sub-au to tens of au, the case for a planet orbiting at around 10 au from the star HD100546 has been very persuasive. Although the planet itself has not been directly detected, the new 7 mm observations reported here, at 15–50 au resolution, make that case compelling, albeit from an abundance of circumstantial evidence. The effect of the planet on the dust emission from the circumstellar disc is consistent with previously published models of early planetary system evolution. For instance, we find a hole in the disc with a radius of around 25 au, but which is almost twice that inferred from UV–IR observations. Such a size discrepancy agrees with expectation if a planet sculpts the cavity. Other findings from our observations – including those presented in the appendices – also support this scenario, including the following.

(1) The dust grains in the disc have evolved significantly from what would be expected in the ISM. The dust emission spectral index is 2.45 $\pm$ 0.10, and under the assumption the emission is mostly optically thin – supported by spatially resolved data down to 19 GHz – the dust emissivity index is 0.5 $\pm$ 0.1, compared to an ISM figure of $\sim$1.7. For any reasonable grain properties found in the literature, the dust has grown to sizes of at least 10 cm, and possibly up to 100 cm.

(2) The dust mass of the disc within a radius $\leq$100 au is of the order of a Jupiter mass. From other published work, the gas mass within a radius of $\sim$400 au is of a similar magnitude, or at most 10 times greater. Whatever the case, the gas-to-dust mass ratio has seemingly evolved from its ISM value of $\sim$100.

(3) A brightness asymmetry exists between the two sides of the disc along its major axis. We interpret this as a case of pericentre glow, whereby the NW side of the disc is closer to the star and thus is warmer with enhanced thermal dust emission. This in turn is a product of an elliptically orbiting massive body which spends most of its time near its apocentre on the SE side of the disc.

(4) A brightness contrast is seen between the SW and NE sides of the disc, such that the disc overall takes the shape of a horseshoe, with the opening on the ENE side. Such an azimuthal asymmetry seen in the reconstructed image is further supported by non-zero imaginary components of the visibilities on small spatial scales. By analogy with similar transition disc systems, the asymmetry is interpreted as a sign of the large dust grains being trapped in a pressure maximum, in turn a by-product of previous planet formation.

(5) The outer disc radius is wavelength independent from 1 to 16 mm, more consistent with a planet–disc interaction scenario than a radial drift process whereby larger grains – probed by longer wavelength emission – migrate inwards.

We have presented perhaps the most detailed ever single study of a Herbig Be star and its disc, showing the value of conducting observations across a wide spectral range, from the infrared through to true radio regimes. ATCA will thus remain an important facility to complement the flood of data that is already emerging from ALMA on transition (and other) disc systems. Indeed, ATCA will be crucial to both separate the dust and free–free (or other) emission components of these systems, as well as to study the parent star and/or the physical processes occurring in the vicinity of the star–disc–outflow boundaries.

In the case of HD100546 this approach has revealed that it does indeed have a significant outflow of a few $\times$ 10^{-8} $M_\odot$ yr^{-1} – evidenced by the 6 cm radio flux and IR hydrogen recombination lines presented here. A relatively high-mass accretion rate, even up to a few $\times$ 10^{-7} $M_\odot$ yr^{-1}, must accompany this outflow, which means that the few tenths of au radius inner disc, and even the entire cavity out to $\sim$10 au, would be depleted on a time-scale of less than a year. Significant amounts of material must then be passing across the cavity from the outer disc, which planet formation models suggest would be better sustained by a multi- rather than single-planet system within about 10 au.

The passage of such a large amount of material in a relatively short time suggests that the inner regions of the HD100546 disc are highly dynamic. This may be reflected in the many examples of variability phenomena seen for this system, including variable radio emission presented here over time-scales as short as tens of minutes. Frequent collisions may also occur between planetesimal-sized bodies, a possible mechanism behind the production of comet-like dust first detected via ISO observations.

Overall, the properties of HD100546 and its disc suggest that the system has two faces, one of relative youth and another of maturity. Its youth is reflected in parameters such as the inflow/outflow rates, presence of dense molecular gas out to several hundred astronomical unit, and a grain population indicative of growth rather than fragmentation. Its maturity is reflected in the highly processed nature of separate grain populations, including crystalline, cometary-like silicates and KBO-like colours, as well as the large inner cavity likely resulting from past planet formation. Whilst all of this perhaps leaves its age somewhat uncertain, by any (astronomical or other) definition of the word it is truly a 'transition' disc system.

ACKNOWLEDGEMENTS

This research was supported by an Australian Research Council (ARC) Australian Research Fellowship awarded to CMW as part of Discovery Project DP0345227, and subsequently as an ARC Future Fellowship FT100100495. STM acknowledges support from the Swinburne Researcher Development Scheme and Swinburne Special Studies Program. We acknowledge the award of significant amounts of observing time for this project by the ATNF and NANTEN2 Time Assignment Committees. The assistance of Paul Jones and Balthasar Indermuhle in conducting the 2012 May and June 7 mm observations is greatly appreciated. We thank the ATNF staff at Narrabri for their hospitality, assistance and patience, especially Robin Wark, Bob Sault and Phil Edwards. We also thank Hiroaki Yamamoto for assistance during the period over which the NANTEN2 observations were performed, and providing 'first look' spectra. We acknowledge the contribution of Tony Wong, particularly his very user-friendly MIRIAD script for reducing ATCA data. We thank Sean Andrews for providing the IDL script to perform the visibility deprojections. Finally, we appreciate the patience of the referee in reviewing such a long paper. This research has made use of the EOD and the Exoplanet Data Explorer at exoplanets.org. This research has made use of the SIMBAD data base operated at CDS, Strasbourg, France.

REFERENCES

Acke B., van den Ancker M. E., 2006, A&A, 449, 267
Acke B., Waelkens C., 2004, A&A, 427, 1009
Acke B., van den Ancker M. E., Dullemond C. P., van Boekel R., Waters L. B. F. M., 2004, A&A, 422, 621
Akeson R. L. et al., 2005, ApJ, 622, 440
Allard F., Hauschildt P. H., Alexander D. R., Tamani A., Schweitzer A., 2001, ApJ, 556, 357

Allard F., Homeier D., Freytag B., 2012, Phil. Trans. R. Soc. A, 370, 2765
Andrews S. M., 2013, in Booth M., Matthews B. C., Graham J. R., eds, Proc. IAU Symp 299, Exploring the Formation and Evolution of Planetary Systems. Cambridge Univ. Press, Cambridge, p. 80
Andrews S. M., Wilner D. J., Hughes A. M., Qi C., Dullemond C. P., 2009, ApJ, 700, 1502
Andrews S. M., Wilner D. J., Hughes A. M., Qi C., Dullemond C. P., 2010, ApJ, 723, 1241
Andrews S. M., Wilner D. J., Espaillat C., Hughes A. M., Dullemond C. P., McClure M. K., Qi C., Brown J. M., 2011a, ApJ, 732, 42
Andrews S. M., Rosenfeld K. A., Wilner D. J., Bremer M., 2011b, ApJ, 742, L5
Andrews S. M. et al., 2012, ApJ, 744, 162
Apai D. et al., 2008, ApJ, 672, 1196
Ardila D. R., Golimowski D. A., Krist J. E., Clampin M., Ford H. C., Illingworth G. D., 2007, ApJ, 665, 512
Ataiee S., Pinilla P., Zsom A., Dullemond C. P., Dominik C., Ghanbari J., 2013, A&A, 553, L3
Augereau J. C., Lagrange A. M., Mouillet D., Ménard F., 2001, A&A, 365, 78
Avenhaus H., Quanz S. P., Schmid H. M., Meyer M. R., Garufi A., Wolf S., Dominik C., 2014a, ApJ, 781, 87
Avenhaus H., Quanz S. P., Meyer M. R., Brittain S. D., Carr J. S., Najita J. R., 2014b, ApJ, 790, 56
Bagnulo S., Landstreet J. D., Fossati L., Kochukhov O., 2012, A&A, 538, A129
Banzatti A., Testi L., Isella A., Natta A., Neri R., Wilner D. J., 2011, A&A, 525, A12
Baraffe I., Chabrier G., Barman T. S., Allard F., Hauschildt P. H., 2003, A&A, 402, 701
Beckwith S. V. W., Sargent A. I., 1991, ApJ, 381, 250
Benedettini M., Nisini B., Giannini T., Lorenzetti D., Tommasi E., Saraceno P., Smith H. A., 1998, A&A, 339, 159
Benedettini M., Pezzuto S., Giannini T., Lorenzetti D., Nisini B., 2001, A&A, 379, 557
Benisty M., Tatulli E., Menard F., Swain M. R., 2010, A&A, 511, A75
Berger J. P., Segransan D., 2007, New Astron. Rev., 51, 576
Beust H., Karmann C., Lagrange A.-M., 2001, A&A, 366, 945
Biller B. et al., 2012, ApJ, 753, L38
Biller B. A. et al., 2013, ApJ, 777, 160
Biller B. A. et al., 2014, ApJ, 792, L22
Birnstiel T., Andrews S. M., 2014, ApJ, 780, 153
Birnstiel T. et al., 2010, A&A, 516, L14
Birnstiel T., Dullemond C. P., Pinilla P., 2013, A&A, 550, L8
Blondel P. F.C, Tjin A., Djie H. R. E., 2006, A&A, 456, 1045
Boccaletti A., Pantin E., Lagrange A.-M, Augereau J.-C., Meheut H., Quanz S. P., 2013, A&A, 560, A20
Bonavita M. et al., 2010, A&A, 522, A2
Bouwman J., de Koter A., Dominik C., Waters L. B. F. M., 2003, A&A, 401, 577
Brandt T. D. et al., 2014, ApJ, 794, 159
Brittain S. D., Najita J. R., Carr J. S., 2009, ApJ, 702, 85
Brittain S. D., Najita J. R., Carr J. S., Liskowsky J., Troutman M. R., Doppmann G. W., 2013, ApJ, 767, 159
Brittain S. D., Carr J. S., Najita J. R., Quanz S. P., Meyer M. R., 2014, ApJ, 791, 136
Brown J. M. et al., 2007, ApJ, 664, L107
Brown J. M., Blake G. A., Qi C., Dullemond C. P., Wilner D. J., 2008, ApJ, 675, L109
Brown J. M., Blake G. A., Qi C., Dullemond C. P., Wilner D. J., Williams J. P., 2009, ApJ, 704, 496
Brown J. M., Herczeg G. J., Pontoppidan K. M., van Dishoeck E. F., 2012, ApJ, 744, 116
Bruderer S., van Dishoeck E. F., Doty S. D., Herczeg G. J., 2012, A&A, 541, A91
Bruderer S., van der Marel N., van Dishoeck E. F., van Kempen T. A., 2014, A&A, 562, A26
Calvet N., 2004, in Dupree A. K., Benz A. O., eds, Proc. IAU Symp. 219, Stars as Suns: Activity, Evolution and Planets. Astron. Soc. Pac., San Francisco, p. 599
Calvet N., Muzerolle J., Briceno C., Hernandez J., Hartmann L, Saucedo J. L., Gordon K. D., 2004, AJ, 128, 1294
Calvet N. et al., 2005, ApJ, 630, L185
Canovas H. et al., 2015, ApJ, 805, 21
Carmona A., van der Plas G., van den Ancker M. E., Audard M., Waters L. B. F. M., Fedele D., Acke B., Pantin E., 2011, A&A, 533, A39
Casassus S., Perez S. M., Jordan A., Menard F., Cuadra J., Schreiber M. R., Hales A. S., Ercolano B., 2012, ApJ, 754, L31
Casassus S. et al., 2013, Nature, 493, 191
Chabrier G., Baraffe I., Allard F., Hauschildt P., 2000, ApJ, 542, 464
Chauvin G. et al., 2015, A&A, 573, A127
Cheetham A., Huelamo N., Lacour S., de Gregorio-Monsalvo I., Tuthill P., 2015, MNRAS, 450, L1
Cieza L. A. et al., 2012, ApJ, 752, 75
Clarke D., Smith R. A., Yudin R. V., 1999, A&A, 347, 590
Close L. M. et al., 2014, ApJ, 781, L30
Costigan G., Vink J. S., Scholz A., Ray T., Testi L., 2014, MNRAS, 440, 3444
Currie T. et al., 2014, ApJ, 796, L30
D'Alessio P., Calvet N., Hartmann L., Lizano S., Canto J., 1999, ApJ, 527, 893
D'Alessio P., Merin B., Calvet N., Hartmann L., Montesinos B., 2005, Rev. Mex. Astron. Astrofis., 41, 61
de Juan Ovelar M., Min M., Dominik C., Thalmann C., Pinilla P., Benisty M., Birnstiel T., 2013, A&A, 560, A111
Deleuil M., Lecavelier des Etangs A., Bouret J.-C., Roberge A., Vidal-Madjar A., Martin C., Feldman P. D., Ferlet R., 2004, A&A, 418, 577
Devine D., Grady C. A., Kimble R. A., Woodgate B., Bruhweiler F. C., Boggess A., Linsky J. L., Clampin M., 2000, ApJ, 542, L115
Dodson-Robinson S. E., Salyk C., 2011, ApJ, 738, 131
Dodson-Robinson S. E., Veras D., Ford E. B., Beichman C. A., 2009, ApJ, 707, 79
Doering R. L., 2008, PhD thesis, Univ. Illinois
Dominik C., Dullemond C. P., Waters L. B. F. M., Walch S., 2003, A&A, 398, 607
Donati J.-F., Semel M., Carter B. D., Rees D. E., Cameron A. C., 1997, MNRAS, 291, 658
Donehew B., Brittain S., 2011, AJ, 141, 46
Dong R. et al., 2012, ApJ, 750, 161
Draine B. T., 2006, ApJ, 636, 1114
Dullemond C. P., Dominik C., 2005, A&A, 434, 971
Dutrey A. et al., 2008, A&A, 490, L15
Eisner J. A., Lane B. F., Hillenbrand L. A., Akeson R. L., Sargent A. I., 2004, ApJ, 613, 1049
Eisner J. A., Monnier J. D., Tuthill P., Lacour S., 2009, ApJ, 698, L169
Elia D., Strafella F., Campeggio L., Giannini T., Lorenzetti D., Nisini B., Pezzuto S., 2004, ApJ, 601, 1000
Espaillat C. et al., 2010, ApJ, 717, 441
Espaillat C., Furlan E., D'Alessio P., Sargent B., Nagel E., Calvet N., Watson D. M., Muzerolle J., 2011, ApJ, 728, 49
Evans T. M. et al., 2012, ApJ, 744, 120
Fedele D., Bruderer S., van Dishoeck E. F., Hogerheijde M. R., Panic O., Brown J. M., Henning Th., 2013, ApJ, 776, L3
Follette K. B. et al., 2013, ApJ, 767, 10
Follette K. et al., 2015, ApJ, 798, 132
France K. et al., 2012, ApJ, 756, 171
Fu W., Li H., Lubow S., Li S., 2014, ApJ, 788, L41
Fukagawa M. et al., 2013, PASJ, 65, L14
Garcia Lopez R., Natta A., Testi L., Habart E., 2006, A&A, 459, 837
Garufi A. et al., 2013, A&A, 560, A105
Garufi A. et al., 2014, A&A, 567, A141
Geers V. C., van Dishoeck E. F., Visser R., Pontoppidan K. M., Augereau J.-C., Habart E., Lagrange A. M., 2007, A&A, 476, 279
Ghez A. M., Neugebauer G., Matthews K., 1993, AJ, 106, 2005

Grady C. A., Sitko M. L., Bjorkman K. S., Perez M. R., Lynch D. K., Russell R. W., Hanner M. S., 1997, ApJ, 483, 449
Grady C. A. et al., 2001, AJ, 122, 3396
Grady C. A. et al., 2004, ApJ, 608, 809
Grady C. A., Woodgate B., Heap S. R., Bowers C., Nuth J. A., Herczeg G. J., Hill H. G. M., 2005, ApJ, 620, 470
Grady C. A. et al., 2007, ApJ, 665, 1391
Grady C. A. et al., 2009, ApJ, 699, 1822
Grady C. A. et al., 2013, ApJ, 762, 48
Gräfe C., Wolf S., Roccatagliata V., Sauter J., Ertel S., 2011, A&A, 533, A89
Grether D., Lineweaver C. H., 2006, ApJ, 640, 1051
Güdel M., 2002, ARA&A, 40, 217
Guilloteau S., Dutrey A., Simon M., 1999, A&A, 348, 570
Guilloteau S., Dutrey A., Pietu V., Boehler Y., 2011, A&A, 529, A105
Guimaraes M. M., Alencar S. H. P., Corradi W. J. B., Vieira S. L. A., 2006, A&A, 457, 581
Gullbring E., Hartmann L, Briceno C., Calvet N., 1998, ApJ, 492, 323
Habart E., Natta A., Testi L., Carbillet M., 2006, A&A, 449, 1067
Hamidouche M., Wang S., Looney L. W., 2008, AJ, 135, 1474
Harker D. E., Woodward C. E., Wooden D. H., Temi P., 2005, ApJ, 622, 430
Hartmann L., Calvet N., Gullbring E., D'Alessio P., 1998, ApJ, 495, 385
Hashimoto J. et al., 2012, ApJ, 758, L19
Hashimoto J. et al., 2013, ApJ, 775, L33
Henning Th., Launhardt R., Steinacker J., Thamm E., 1994, A&A, 291, 546
Henning Th., Burkert A., Launhardt R., Leinert Ch., Stecklum B., 1998, A&A, 336, 565
Honda M. et al., 2012, ApJ, 752, 143
Hu J. Y., The P. S., de Winter D., 1989, A&A, 208, 213
Hubrig S. et al., 2009, A&A, 502, 283
Hubrig S., Ilyin I., Schöller M., Lo Curto G., 2013, Astron. Nachr., 334, 1093
Huelamo N., Lacour S., Tuthill P., Ireland M., Kraus A., Chauvin G., 2011, A&A, 528, L7
Huelamo N., de Gregorio-Monsalvo I., Macias E., Pinte C., Ireland M., Tuthill P., Lacour S., 2015, A&A, 575, L5
Hughes A. M., Wilner D. J., Calvet N., D'Alessio P., Claussen M. J., Hogerheijde M. R., 2007, ApJ, 664, 536
Hughes A. M., Wilner D. J., Qi C., Hogerheijde M. R., 2008, ApJ, 678, 1119
Hughes A. M. et al., 2009, ApJ, 698, 131
Hummer D. G., Storey P. J., 1987, MNRAS, 224, 801
Indermuehle B. T., Burton M. G., 2014, PASA, 31, 32
Ingleby L. et al., 2013, ApJ, 767, 112
Ireland M. J., Kraus A. L., 2013, in Booth M., Matthews B. C., Graham J. R., eds, Proc. IAU Symp. 299, Exploring the Formation and Evolution of Planetary Systems. Cambridge Univ. Press, Cambridge, p. 199
Ireland M. J., Kraus A., Martinache F., Law N., Hillenbrand L. A., 2011, ApJ, 726, 113
Isella A., Tatulli E., Natta A., Testi L., 2008, A&A, 483, L13
Isella A., Carpenter J. M., Sargent A. I., 2009, ApJ, 701, 260
Isella A., Carpenter J. M., Sargent A. I., 2010a, ApJ, 714, 1746
Isella A., Natta A., Wilner D. J., Carpenter J. M., Testi L., 2010b, ApJ, 725, 1735
Isella A., Perez L. M., Carpenter J. M., Ricci L., Andrews S., Rosenfeld K., 2013, ApJ, 775, 30
Isella A., Chandler C. J., Carpenter J. M., Perez L. M., Ricci L., 2014, ApJ, 788, 129
Janson M., Bonavita M., Klahr H., Lafreniere D., Jayawardhana R., Zinnecker H., 2011, ApJ, 736, 89
Janson M. et al., 2013, ApJ, 773, 73
Jones P., Indermuehle B., Burton M., 2012, UNSW Report on Water Vapour Radiometer Correction of ATCA Data
Kley W., Dirksen G., 2006, A&A, 447, 369
Kouwenhoven M. B. N., Brown A. G. A., Kaper L., 2007, A&A, 464, 581
Kraus A. K., Ireland M. J., 2010, in Corbett I. F., ed., XXVIIth IAU General Assembly, Highlights of Astronomy, Volume 15. Cambridge Univ. Press, Cambridge p. 766
Kraus A. K., Ireland M. J., 2012, ApJ, 745, 5
Kraus A. L., Ireland M. J., Martinache F., Lloyd J. P., 2008, ApJ, 679, 762
Kraus A. L., Ireland M. J., Martinache F., Hillenbrand L. A., 2011, ApJ, 731, 8
Ladd N., Purcell C., Wong T., Robertson S., 2005, PASA, 22, 62
Lafreniere D. et al., 2007, ApJ, 670, 1367
Lazareff B. et al., 2013, in Arnold L., Le Coroller H., Surdej J., eds, Proceedings of Haute Provence Observatory Colloquium, Improving the Performances of Current Optical Interferometers & Future Designs. p. 111, available at: http://interferometer.osupytheas.fr/index.php
Leinert Ch. et al., 2004, A&A, 423, 537
Levenhagen R. S., Leister N. V., 2004, AJ, 127, 1176
Liskowsky J. P., Brittain S. D., Najita J. R., Carr J. S., Doppmann G. W., Troutman M. R., 2012, ApJ, 760, 153
Liu W. M., Hinz P. M., Meyer M. R., Mamajek E. E., Hoffmann W. F., Hora J. L., 2003, ApJ, 598, L111
Liu W. M., Hinz P. M., Meyer M. R., Mamajek E. E., Hoffmann W. F., Brusa G., Miller D., Kenworthy M. A., 2007, ApJ, 658, 1164
Lommen D. et al., 2007, A&A, 462, 211
Lommen D., Maddison S. T., Wright C. M., van Dishoeck E. F., Wilner D. J., Bourke T. L., 2009, A&A, 495, 869
Lowrance P. J. et al., 2005, AJ, 130, 1845
Lyo A.-R., Ohashi N., Qi C., Wilner D. J., Su Y.-N., 2011, AJ, 142, 151
Ma B., Ge J., 2014, MNRAS, 439, 2781
Maaskant K. M. et al., 2013, A&A, 555, A64
Malfait K., Bogaert E., Waelkens C., 1998a, A&A, 331, 211
Malfait K., Waelkens C., Waters L. B. F. M., Vandenbussche B., Huygen E., de Graauw M. S., 1998b, A&A, 332, L25
Manara C. F., Testi L., Natta A., Rosotti G., Benisty M., Ercolano B., Ricci L., 2014, A&A, 568, A18
Manoj P., Bhatt H. C., Maheswar G., Muneer S., 2006, ApJ, 653, 657
Marino S., Casassus S., Lacour S., Pinte C., Thiebaut E., 2014a, poster paper at conference on Herbig Ae/Be stars: The missing link in star formation. Available at: http://www.eso.org/sci/meetings/2014/Haebe2014/Contributions/Posters/Marino.pdf
Marino S., Casassus S., Lacour S., Pinte C., Thiebaut E., 2014b, poster paper at conference on Characterizing Planetary Systems Across the HR Diagram. Available at: http://www.ast.cam.ac.uk/sites/default/files/talk_archive/Marino_acrossHR_poster.pdf
Mathews G. S., Williams J. P., Menard F., 2012, ApJ, 753, 59
Mayama S. et al., 2012, ApJ, 760, L26
Mendigutia I., Calvet N., Montesinos B., Mora A., Muzerolle J., Eiroa C., Oudmaijer R. D., Merin B., 2011, A&A, 535, A99
Mendigutia I., Fairlamb J., Montesinos B., Oudmaijer R. D., Najita J. R., Brittain S. D., van den Ancker M. E., 2014, ApJ, 790, 21
Merin B. et al., 2004, A&A, 419, 301
Merin B. et al., 2010, ApJ, 718, 1200
Metchev S. A., Hillenbrand L. A., 2009, ApJS, 181, 62
Middleberg E., Sault R. J., Kesteven M. J., 2006, PASA, 23, 147
Miyake K., Nakagawa Y., 1993, Icarus, 106, 20
Mulders G. D. et al., 2011, A&A, 531, A93
Mulders G. D., Min M., Dominik C., Debes J. H., Schneider G., 2013a, A&A, 549, A112
Mulders G. D., Paardekooper S.-J., Panic O., Dominik C., van Boekel R., Ratzka T., 2013b, A&A, 557, A68
Muto T. et al., 2012, ApJ, 748, L22
Najita J. R., Andrews S. M., Muzerolle J., 2007, MNRAS, 378, 369
Natta A., Testi L., 2004, in Johnstone D., Adams F. C., Lin D. N. C., Neufeld D. A., Ostriker E. C., eds, ASP Conf. Ser. Vol. 323, Star Formation in the Interstellar Medium. Astron. Soc. Pac., San Francisco, p. 279
Natta A., Testi L., Neri R., Shepherd D. S., Wilner D. J., 2004, A&A, 416, 179
Natta A., Testi L., Randich S., 2006, A&A, 452, 245
Natta A., Testi L., Calvet N., Henning Th., Waters L. B. F. M., Wilner D. J., 2007, in Reipurth B., Jewitt D., Keil K., eds, ASP Conf. Ser. Vol. 951, Protostars and Planets V. Astron. Soc. Pac., San Francisco, p. 767
Nielsen E. L., Close L. M., 2010, ApJ, 717, 878
Nielsen E. L., Close L. M., Biller B. A., Masciadri E., Lenzen R., 2008, ApJ, 674, 466

Nielsen E. L. et al., 2013, ApJ, 776, 4
Nisini B., Milillo A., Saraceno P., Vitali F., 1995, A&A, 302, 169
Ohashi N., 2008, Ap&SS, 313, 101
Olofsson J. et al., 2011, A&A, 528, L6
Olofsson J. et al., 2013, A&A, 552, A4
Orellana M., Cieza L. A., Schreiber M. R., Merin B., Brown J. M., Pellizza L. J., Romero G. A., 2012, A&A, 539, A41
Osorio M. et al., 2014, ApJ, 791, L36
Otrupcek R. E., Hartley M., Wang J.-S., 2000, PASA, 17, 92
Panagia N., Felli M., 1975, A&A, 39, 1
Panic O., Hogerheijde M. R., 2009, A&A, 508, 707
Panic O., van Dishoeck E. F., Hogerheijde M. R., Belloche A., Gusten R., Boland W., Baryshev A., 2010, A&A, 519, A110
Panic O., Ratzka Th., Mulders G. D., Dominik C., van Boekel R., Henning Th., Jaffe W., Min M., 2014, A&A, 562, A101
Pantin E., Waelkens C., Lagage P. O., 2000, A&A, 361, L9
Perez L. M. et al., 2010, ApJ, 724, 493
Perez L. M. et al., 2012, ApJ, 760, L17
Perez L. M., Isella A., Carpenter J. M., Chandler C. J., 2014, ApJ, 783, L13
Perez S. et al., 2015, ApJ, 798, 85
Pietu V., Dutrey A., Guilloteau S., Chapillon E., Pety J., 2006, A&A, 460, L43
Pietu V., Dutrey A., Guilloteau S., 2007, A&A, 467, 163
Pietu V., Guilloteau S., Di Dolco E., Dutrey A., Boehler Y., 2014, A&A, 564, A95
Pineda J. E., Quanz S. P., Meru F., Mulders G. D., Meyer M. R., Panic O., Avenhaus H., 2014, ApJ, 788, L34
Pinilla P., Benisty M., Birnstiel T., 2012, A&A, 545, A81
Pinilla P. et al., 2014, A&A, 564, A51
Pinilla P., Birnstiel T., Walsh C., 2015, A&A, in press
Pogodin M. A., 1995, Ap&SS, 224, 539
Pogodin M. A., Hubrig S., Yudin R. V., Scholler M., Gonzalez J. F., Stelzer B., 2012, Astron. Nachr., 333, 594
Pollack J. B., Hollenbach D., Beckwith S., Simonelli D. P., Roush T., Fong W., 1994, ApJ, 421, 615
Pontoppidan K. M., Blake G. A., van Dishoeck E. F., Smette A., Ireland M. J., Brown J., 2008, ApJ, 684, 1323
Pontoppidan K. M., Blake G. A., Smette A., 2011, ApJ, 733, 84
Pott J.-U., Perrin M. D., Furlan E., Ghez A. M., Herbst T. M., Metchev S., 2010, ApJ, 710, 265
Quanz S. P., Schmid H. M., Geissler K., Meyer M. R., Henning Th., Brandner W., Wolf S., 2011, ApJ, 738, 23
Quanz S. P., Amara A., Meyer M. R., Kenworthy M. A., Kasper M., Girard J. H., 2013a, ApJ, 766, L1
Quanz S. P., Avenhaus H., Buenzli E., Garufi A., Schmid H. M., Wolf S., 2013b, ApJ, 766, L2
Quanz S. P., Amara A., Meyer M. R., Girard J. H., Kenworthy M. A., Kasper M., 2015, ApJ, 807, 64
Quillen A. C., 2006, ApJ, 640, 1078
Rameau J., Chauvin G., Lagrange A.-M., Thebault P., Milli J., Girard J. H., Bonnefoy M., 2012, A&A, 546, A24
Randich M. S., Giovanardi C., Natta A., Palla F., 1991, A&AS, 88, 31
Ratzka T., Kohler R., Leinert Ch., 2005, A&A, 437, 611
Regaly Zs., Juhasz A., Sandor Zs., Dullemond C. P., 2012, MNRAS, 419, 1701
Reggiani M. et al., 2014, ApJ, 792, L23
Riaud P., Mawet D., Absil O., Boccaletti A., Baudoz P., Herwats E., Surdej J., 2006, A&A, 458, 317
Ricci L., Trotta F., Testi L., Natta A., Isella A., Wilner D. J., 2012, A&A, 540, A6
Rodigas T. J., Follette K. B., Weinberger A., Close L., Hines D. C., 2014, ApJ, 791, L37
Rodmann J., Henning Th., Chandler C. J., Mundy L. G., Wilner D. J., 2006, A&A, 446, 211
Romero G., Schreiber M. R., Cieza L. A., Rebassa-Mansergas A., Merin B., Smith Castelli A. V., Allen L. E., Morrell N., 2012, ApJ, 749, 79
Sallum S. et al., 2015, ApJ, 801, 85
Salyk C., Herczeg G. J., Brown J. M., Blake G. A., Pontoppidan K. M., van Dishoeck E. F., 2013, ApJ, 769, 21
Sault R. J., Teuben P. J., Wright M. C. H., 1995, in Shaw R. A., Payne H. E., Hayes J. J. E., eds, ASP Conf. Ser. Vol. 77,Astronomical Data Analysis Software and Systems IV. Astron. Soc. Pac. San Francisco, p. 433
Simon M., Felli M., Cassar L., Fischer J., Massi M., 1983, ApJ, 266, 623
Simon M. et al., 1995, ApJ, 443, 625
Skinner S. L., Brown A., Stewart R. T., 1993, ApJS, 87, 217
Skinner S. L., Güdel M., Audard M., Smith K., 2004, ApJ, 614, 221
Spiegel D. S., Burrows A., 2012, ApJ, 745, 174
Stelzer B., Micela K., Hamaguchi K., Schmitt J. H. M. M., 2006, A&A, 457, 223
Takami M. et al., 2013, ApJ, 772, 145
Talavera A., Blondel P. F. C., Tjin A., Djie H. R. E., 1994, in The P. S., Perez M. R., van den Heuvel E. P. J., eds, ASP Conf. Ser. Vol. 62, The Nature and Evolutionary Status of Herbig Ae/Be Stars. Astron. Soc. Pac., San Francisco, p. 115
Tanii R. et al., 2012, PASJ, 64, 124
Tatulli E. et al., 2011, A&A, 531, A1
Telesco C. M. et al., 2000, ApJ, 530, 329
Testi L. et al., 2014, in Beuther H., Klessen R., Dullemond C., Henning Th., eds, Protostars and Planets VI. Univ. Arizona Press, Tucson, AZ, p. 339
Thalmann C. et al., 2010, ApJ, 718, L87
Thalmann C. et al., 2014, A&A, 566, A51
Torniainen I., Tornikovski M., Terasranta H., Aller M. F., Aller H. D., 2005, A&A, 435, 839
Trotta F., Testi L., Natta A., Isella A., Ricci L., 2013, A&A, 558, A64
Tsukagoshi T. et al., 2014, ApJ, 783, 90
Ubach C., Maddison S. T., Wright C. M., Wilner D. J., Lommen D. J. P., Koribalski B., 2012, MNRAS, 425, 3137
Valenti J. A., Basri G., Johns C. M., 1993, AJ, 106, 2024
van den Ancker M. E., The P. S., Tjin A Djie H. R. E., Catala C., de Winter D., Blondel P. F. C., Waters L. B. F. M., 1997, A&A, 324, L33
van den Ancker M. E., Wesselius P. R., Tielens A. G. G. M., 2000, A&A, 355, 194
van der Marel N. et al., 2013, Science, 340, 1199
van der Marel N., van Dishoeck E. F., Bruderer S., Perez L. M., Isella A., 2015, A&A, 579, A106
van der Plas G., van den Ancker M. E., Acke B., Carmona A., Dominik C., Fedele D., Waters L. B. F. M., 2009, A&A, 500 1137
van Leeuwen F., 2007, A&A, 474, 653
Verhoeff A. P. et al., 2011, A&A, 528, A91
Vicente S. et al., 2011, A&A, 533, A135
Vieira S. L. A., Pogodin M. A., Franco G. A. P., 1999, A&A, 345, 559
Vigan A. et al., 2012, A&A, 544, A9
Wade G. A., Bagnulo S., Drouin D., Landstreet J. D., Monin D., 2007, MNRAS, 376, 1145
Wahhaj Z. et al., 2013, ApJ, 773, 179
Walsh C. et al., 2014, ApJ, 791, L6
White R. J., Ghez A. M., 2001, ApJ, 556, 265
Wilner D. L., Bourke T. L., Wright C. M., Jørgensen J. K., van Dishoeck E. F., Wong T., 2003, ApJ, 596, 597
Wilson W. E. et al., 2011, MNRAS, 416, 832
Wright J. T. et al., 2011, PASP, 123, 412
Wyatt M. C., Dermott S. F., Telesco C. M., Fisher R. S., Grogan K., Holmes E. K., Pina R. K., 1999, ApJ, 527, 918
Yudin R. V., Evans A., 1998, A&AS, 131, 401
Zhang K., Isella A., Carpenter J. M., Blake G. A., 2014, ApJ, 791, 42
Zhu Z., Nelson R.P, Hartmann L, Espaillat C., Calvet N., 2011, ApJ, 729, 47

SUPPORTING INFORMATION

Additional Supporting Information may be found in the online version of this article:

HD100546_CMWrightetal_OnlineOnly.pdf
(http://mnras.oxfordjournals.org/lookup/suppl/doi:10.1093/mnras/stv1619/-/DC1).

APPENDIX A: HD100546 ATCA FLUXES AND IMAGES AT 3, 16, 35 AND 62 MM

This appendix is supplementary material and only available with the online version of the paper.

APPENDIX B: MOLECULAR GAS – ATCA HCO+ $J = 1 \rightarrow 0$ AND NANTEN2 CO $J = 7 \rightarrow 6$ AND $4 \rightarrow 3$

This appendix is supplementary material and only available with the online version of the paper.

APPENDIX C: EMISSION ORIGIN AT CENTIMETRE WAVELENGTHS

This appendix is supplementary material and only available with the online version of the paper.

APPENDIX D: CENTIMETRE TEMPORAL MONITORING

This appendix is supplementary material and only available with the online version of the paper.

APPENDIX E: REFERENCES FOR STELLAR AND DISC PARAMETERS IN TABLE 3

References are given here for the stellar and disc properties of each transition disc system included in Table 3.

Stellar properties (distance, age, mass and accretion rate) are taken from

Costigan et al. (2014) for RY Tau, UX Tau A, BP Tau

Garufi et al. (2014) for FT Tau

Manara et al. (2014) for LkHα 330, DM Tau, LkCa 15, GM Aur, RX J1615, SR 21, WSB 60, DoAr 44

Mendigutia et al. (2014) for HD142527

Ingleby et al. (2013) for BP Tau, DM Tau, GM Aur, LkCa 15

Salyk et al. (2013) for CI Tau

Donehew & Brittain (2011) for CQ Tau, MWC 758

Mendigutia et al. (2011) for CQ Tau, RY Tau

Pogodin et al. (2012) for HD100546, HD135344B

Espaillat et al. (2010) for LkCa 15, DoAr 44, UX Tau A

Isella, Carpenter & Sargent (2009) for DM Tau, LkCa 15, RY Tau, GM Aur, SR 24 S

Najita, Andrews & Muzerolle (2007) for UX Tau A

Blondel & Tjin A Djie (2006) for HD169142, MWC 758, CQ Tau

Garcia Lopez et al. (2006) for HD169142, HD135344B, HD142527, CQ Tau

Natta, Testi & Randich (2006) for SR 24S, SR 21, WSB 60

Calvet et al. (2005) for DM Tau, GM Aur

Calvet et al. (2004) for RY Tau

White & Ghez (2001) for GM Aur, DS Tau, LkCa 15, BP Tau, CI Tau, DM Tau

Gullbring et al. (1998) for BP Tau, DS Tau, GM Aur

Hartmann et al. (1998) for BP Tau, DS Tau, GM Aur, CI Tau, DM Tau, LkCa 15

Valenti, Basri & Johns (1993) for BP Tau, CI Tau, DM Tau, DS Tau, GM Aur.

Disc properties (visibility nulls, radius in large dust, small dust and gas tracers), plus some stellar properties, are taken from

Canovas et al. (2015), Tsukagoshi et al. (2014), Romero et al. (2012) for Sz 91

Follette et al. (2015), Bruderer et al. (2014), van der Marel et al. (2013), Brown et al. (2012), Geers et al. (2007) for Oph IRS48

Huelamo et al. (2015), Olofsson et al. (2011) for T Cha

Perez et al. (2015), Avenhaus et al. (2014b), Casassus et al. (2013), Fukagawa et al. (2013), Casassus et al. (2012), Verhoeff et al. (2011), Ohashi (2008), Casassus & Wright et al. (in preparation, for first visibility null at 34 GHz) for HD142527

van der Marel et al. (2015) for SR 21, HD135344B, LkCa 15, RX J1615-3255, SR 24 S, J1604-2130

Isella et al. (2014), Thalmann et al. (2014), Andrews et al. (2011b), Pietu, Dutrey & Guilloteau (2007) and Pietu et al. (2006) for LkCa 15

Osorio et al. (2014), Quanz et al. (2013b), Honda et al. (2012) for HD169142

Perez et al. (2014) for HD135344B, SR 21

Pietu et al. (2014) for DS Tau

Zhang et al. (2014), Mathews, Williams & Menard (2012), Mayama et al. (2012) for J160421.7-213028

Follette et al. (2013), Pontoppidan et al. (2008), Eisner et al. (2009) for SR 21

Garufi et al. (2013), Muto et al. (2012), Lyo et al. (2011), Pontoppidan et al. (2008) for HD135344B

Isella et al. (2013), Pontoppidan et al. (2011), Brown et al. (2008) for LkHα 330

Maaskant et al. (2013) for HD169142, HD135344B, Oph IRS48

Takami et al. (2013), Isella, Carpenter & Sargent (2010a), Akeson et al. (2005) for RY Tau

Trotta et al. (2013), Banzatti et al. (2011) for CQ Tau

Cieza et al. (2012), Orellana et al. (2012) for J1633.9-2422

Dong et al. (2012), Hashimoto et al. (2013, 2012) for PDS 70

France et al. (2012) for BP Tau, DM Tau, GM Aur, HD135344B, LkCa 15, UX Tau A

Tanii et al. (2012) for UX Tau A

Andrews et al. (2011a) for MWC 758, HD135344B, LkHα 330, SR 21, UX Tau A, SR 24 S, DoAr 44, LkCa 15, RX J1615-3255, GM Aur, DM Tau, WSB 60

Espaillat et al. (2011) for DM Tau, GM Aur, LkCa 15, RY Tau, UX Tau A

Gräfe et al. (2011) for DM Tau, GM Aur

Guilloteau et al. (2011) for BP Tau, CI Tau, CQ Tau, DM Tau, FT Tau, GM Aur, LkCa 15, MWC 758

Andrews et al. (2010) for SR 24 S

Espaillat et al. (2010) for LkCa 15, UX Tau A, DoAr 44, GM Aur, DM Tau

Isella et al. (2010b), Isella et al. (2008) for MWC 758

Merin et al. (2010) for RX J1615.3-3255

Andrews et al. (2009) for SR 21, WSB 60, DoAr 44

Brown et al. (2009) for LkHα 330, SR 21 N, HD135344B

Hughes et al. (2009), Dutrey et al. (2008) for GM Aur

Brown et al. (2007) for LkHα 330, SR 21 N, HD135344B, T Cha

Eisner et al. (2004) for MWC 758, CQ Tau

This paper has been typeset from a TEX/LATEX file prepared by the author.